Research Paper

Dynamic modelling and simulation of the Graz Cycle for a renewable energy system

Benjamin Mitterrutzner [a,b,*], Lars O. Nord [a], Mohammad A. Motamed [a], Wolfgang Sanz [b]

[a] *Department of Energy and Process Engineering, NTNU - Norwegian University of Science and Technology, Trondheim, Norway*
[b] *Institute of Thermal Turbomachinery and Machine Dynamics, Graz University of Technology, Graz, Austria*

ARTICLE INFO

ABSTRACT

Critical atmospheric carbon dioxide levels and, in response, an increasing shift toward variable renewable energy sources causes the need of transient operation for thermal power plants coupled with carbon capture and storage. In this regard, dynamic process simulations are a valuable tool for predicting the cycling performance of power plants. In this study, the proposed Graz Cycle, an oxy-combustion power plant fired with natural gas, is investigated and modelled in (a) the steady-state design-point (i.e., full-load), (b) steady-state off-design (i.e., part-load), and (c) dynamic conditions. At full loads, the Graz Cycle power plant achieves a maximum net plant efficiency of 54.5%, comparable to the performance results of the competing Allam cycle found in relevant studies. In the off-design simulation, considering for the first time compressor component maps with variable inlet guide vanes, the load is reduced down to 50% achieving improved performance results compared to previous studies. The dynamic simulation boils down to a ramp rate analysis and shows that practical ramp rates of 5.55 %/min for load decrease and 18.18 %/min for load increase can be reached. The results show that the high ramp rates of the Graz Cycle enable balancing services to the electrical grid next to clean and dispatchable power generation. In this study, a systematic first-principle modelling approach has been developed with the final aim to evolve dynamic models for oxy-combustion carbon capture cycles, and a first-of-its-kind analysis of the dynamic operation of the Graz Cycle is presented.

1. Introduction

1.1. Path towards carbon capture and storage

Human activities, primarily by burning fossil fuels such as coal, oil and natural gas, have increased the atmospheric greenhouse gases to dangerous levels such that many natural ecosystems are at risk [1]. Among all greenhouse gases which cause the global warming effect, carbon dioxide is the most important one [2]. This is due to the high amount emitted through all carbon conversion processes and to a lesser extent due to its chemical characteristics. Furthermore, the trend of temperature increase is reinforced by a growing population and thus a steeply increasing global energy consumption [3]. Ultimately, the rise in energy demand per head as a consequence of progressive prosperity in the industrialised countries puts a strain on the energy systems [4].

In response, renewable energy sources, e.g., solar and wind power, gain importance and incline to dominate the future power generation

mix [5]. Their variable nature denies any firm capacity, to a greater extent it demands balancing services to the grid such that supply matches demand [6]. The most promising possibilities to overcome these fluctuations and prevent energy curtailment are threefold:

- Energy storage which buffers excess renewable energy and releases it in downtimes. This service could be provided by e.g., battery energy storage systems [7], compressed hydrogen storages [8], compressed air energy storages [9] and pumped-storage hydropower plants [10].
- Grid extension strategies [11] and sector coupling [12] like those of electricity and heat demand.
- Flexible power generation [13] in thermal power plants, which ensures auxiliary services to the electrical grid, and follows the variable load of intermittent renewables.

Nomenclature

Dimensionless numbers

Nu	Nusselt number
Pr	Prandtl number
Re	Reynolds number

Greek symbols

α_i	Inner (tube-side) heat transfer coefficient [W/(m^{2}K)]
α_o	Outer (shell-side) heat transfer coefficient [W/(m^{2}K)]
ΔH_f^0	Standard enthalpy of formation [kJ/mol]
δQ	Heat rate supplied to the system [MW]
δW_t	Thermodynamic work rate supplied to the system [MW]
η_i	Efficiency of component i [–]
η_R	Relative efficiency ratio in off-design [–]
λ_C	Combustion excess air ratio [–]
λ_i	Inner (fluid) thermal conductivity [W/(mK)]
λ_o	Outer (fluid) thermal conductivity [W/(mK)]
λ_w	Tube (wall) thermal resistance [W/(mK)]
μ	Dynamic viscosity [kg/(ms)]
μ_R	Relative mass ratio in compressor off-design [–]
μ_w	Dynamic viscosity at the wall [kg/(ms)]
π	Compressor pressure ratio [bar/bar]
ρ_L	Liquid density [kg/m^3]
ρ_m	Tube metal density [kg/m^3]
$\Theta_{i,j}$	Polynomial coefficient [–]
ζ_C	Combustion heat loss [–]

Latin symbols

A_i	Inner (tube-side) area [m^2]
A_o	Outer (shell-side) area [m^2]
c	Velocity [m/s]
c_p	Specific heat capacity at constant pressure [kJ/(kgK)]
c_v	Specific heat capacity at constant volume [kJ/(kgK)]
d_i	Inner tube diameter [m]
d_o	Outer tube diameter [m]
e_{ex}	External energy rate [kJ/kg]
h	Enthalpy rate [kJ/kg]
k	Heat transfer coefficient [W/(m^{2}K)]
kA	Specific heat exchanger property [W/K]
M	Molecular mass [kg/mol]
m	Mass flow rate [kg/s]
M_G	Gaseous mass holdup [kg]
M_L	Liquid mass holdup [kg]
n	Rotational speed [1/min]
P	Power rate [W]
p	Pressure [bar]
R	Gas constant [J/(kmolK)]
R_r	Ramp rate [MW/min]
T	Temperature [°C]

t	Time [s]
T_m	Tube metal temperature [°C]
u	Internal energy rate [kJ/kg]
V	Volume [m^3]
V_m	Tube metal volume [m^3]
x	Vapour quality [kg/kg]

Subscripts

0	Design point value
C	Compressor
G	Gaseous state/generator
L	Liquid state
m	Mechanical
s	Isentropic
T	Turbine
Tr	Transformer

Superscripts

$\overline{T}$	Mean value of temperature gradient

It is challenging to transition to zero-carbon energy systems relying only on renewable energy sources in the near to medium term [14]. In this regard, carbon capture and storage (CCS) will play an essential role to decarbonise quickly the carbon-intensive power and heat generating sector [15] and provide balancing attendances to the grid [16]. To that end, Bui and Mac Dowell [17] identified higher part-load efficiencies and higher ramp rates as two of the main characteristics of flexible CCS power generation for a dispatchable energy system.

Since the 2020s, CCS technologies gain in momentum. It is particularly reflected in integrated assessment models, claiming CCS in the power sector will reach 430 Mt CO$_2$ captured per year, according to the International Energy Agency (IEA) scenario *Net Zero Emissions by 2050* [18]. This is due to exogenously imposed climate goals and carbon prices, as well as the relatively cheap costs of thermal power plants with CO$_2$ capture. According to Ref. [19], by exclusion of CCS from the decarbonisation scenarios, economic costs increase by up to 140% due to more expensive alternative decarbonisation pathways [20]. In other words, Greig and Uden [21] analysed that achieving the climate goals for the United States would be simply impossible without reliance on carbon capture, utilisation and storage.

Indeed, large point-source CCS could play the role of a *bridging technology* toward 100% renewable energy systems[1] [23]. More precisely, three different CO$_2$ capture routes exist and are in depth analysed in various research streams [24]. Most carbon capture and storage technologies are still at a nascent technology stage and thus further research is necessary. However, at the end of the supply chain, the captured CO$_2$ is then to be stored underground, such as in deep saline formations, to *return* these CO$_2$ emissions to the subsurface in a timely manner [25].

What is the role for oxy-combustion[2] power plants with CO$_2$ capture? Among oxy-combustion CCS prospects a few are named here: Graz Cycle [28], Allam cycle [34], MATIANT cycle [35], SCOC-CC cycle [36], Water cycle [37], and CES cycle [38]. They are all highly

---

[1] Recently, solar photovoltaics and wind power technologies have experienced radical cost reductions [22]. In this perspective, a transition towards 100% renewable energies seems immanent, at least in the medium to long term.

[2] Oxy-combustion is the combustion process in the presence of (almost) pure oxygen. To avoid misconception, the widely used term oxy-fuel is not used. For more information, see Ref. [33].

Table 1
Literature review of the key journal publications about the Graz Cycle power plant.

Authors, Ref.	Year	Journal	Short description	Summary of analysis
Jericha and Göttlich [26]	2002	*ASME: Power for Land, Sea and Air*	Conceptual design of an industrial Graz Cycle power plant	In this analysis a thermodynamic and combustion chamber design evaluation is presented. Despite Jericha et al. worked since 1985 on the Graz Cycle concept, this publication represents an important milestone for the development of this cycle. For the first time a highly efficient natural gas fuelled system based on industrial scale application, which is capable to retain CO_2 from the atmosphere, is launched. The Graz Cycle was then further developed in the upcoming years.
Sanz et al. [27]	2004	*ASME: Power for Land, Sea and Air*	Thermodynamic and economic investigation of the S-Graz Cycle	Here, the Graz Cycle is fired with syngas leading to a net cycle efficiency of 60.3% (based on LHV). Moreover, the layout of the S-Graz Cycle is presented for the first time. The schematic arrangement of the turbomachinery is developed and a brief description of the start-up process is presented.
Sanz et al. [28]	2005	*ASME: Power for Land, Sea and Air*	New thermodynamic and economic analysis of the further developed S-Graz Cycle	In this study, the basic layout of the Graz cycle fired with natural gas is described, which this actual work resorts to. The net cycle efficiency is presented to be 52.6% (LHV). Furthermore, an economic analysis of the Graz Cycle led to low CO_2 mitigation costs in the range of 20 \$/ton CO_2 avoided with emphasis on the high impact of the investment cost structure.
Jericha et al. [29]	2006	*ASME: Power for Land, Sea and Air*	Turbomachinery design investigation of the new modified Graz Cycle	This paper introduces the modified version of the Graz Cycle, which promises to have a net efficiency of 53.12% (LHV). The novelty consists of the introduction of a steam bottoming cycle including a low pressure steam turbine. In this regard, the economic cost evaluation showed similar specific CO_2 avoidance costs compared to the 2005 publication. Besides, a very detailed turbomachinery design concept especially for the high temperature turbines and compressors is introduced.
Sanz et al. [30]	2018	*International Journal of Hydrogen Energy*	Adaptation of the Graz Cycle concept to hydrogen including part-load performance	Here, the Graz Cycle concept is adapted to a hydrogen version (as main fuel input). The ASU remains part of the cycle leading to a working fluid of pure water. Maximum efficiency of the hydrogen Graz Cycle is 68.4% (LHV). Investigation of its part-load behaviour down to 30% was shown to be feasible.
Mitterrutzner et al. [31]	2022	*International Journal of Greenhouse Gas Control*	Off-design analysis and development of control strategies for the Graz Cycle	In this study, three different control schemes are developed and evaluated. For all three operational strategies, the part-load (i.e., off-design) performance is investigated. Moreover, off-design modelling of various cycle concepts are proposed. As a result, the part-load control strategy, where the pressure in the HRSG is allowed to vary, is found the most efficient in terms of part-load performance. It is to be noted that this analysis is built on the 2005 cycle configuration and assumptions.
Gutierrez et al. [32]	2023	*Energy Conversion and Management*	Implementation of a membrane oxygen ASU into the Graz Cycle power plant	This work compares two Graz Cycle configurations integrated with a) cryogenic ASU and b) membrane based ASU. In this regard, two membrane alternatives are identified and compared against the cryogenic option. As a result, the thermal efficiency is improved by 0.61% to 2.30%.

efficient alternatives to absorption-based post-combustion CCS systems, but different in terms of readiness and process engineering. Detailed cycle descriptions, efficiency rankings and economic cost indicators are found in the report by IEAGHG [39]. The basis of oxy-combustion cycles is the recycled stream to the combustor leading to an overlap of the topping Joule–Brayton and the bottoming Clausius–Rankine cycle. Since the process layout is much more intrinsic compared to combined cycle technologies, it is not a-priori given how these systems react dynamically and how they are controlled in a logical manner. One way to categorise oxy-combustion power plants is to look upon the fluid used to moderate the combustion process, whether it is a carbon dioxide stream, a water stream, or a combination of both.

This being said, one oxy-combustion power plant already exists on a pilot plant scale in Texas, United States of America. It employs an Allam cycle technology (operated by the company NET Power), and a few others are planned for the United Kingdom [18]. A few studies indicate that the economic costs are favourable for oxy-combustion CCS systems. According to Kehlhofer et al. [40], the power generation cost per unit of energy produced is similar between oxy-combustion cycles and post-combustion absorption capture systems. However, the expected CO_2 avoidance cost of oxy-combustion systems lies slightly lower to the one of post-combustion systems. In contrast and specifically for natural gas fired power plants, the latter thesis is not confirmed by Kanniche et al. [41].

Here, one of the most promising representatives of oxy-combustion cycles, named the Graz Cycle, is studied. The basic principle of the GC

was developed by H. Jericha in the 1980s and from there on step-by-step improved and further investigated. A literature review based on the development and evolution over the years of this specific cycle is summarised in Table 1.

1.2. Integration of CCS power plants with variable renewable energy sources

Flexibility services to the grid gain importance due to deep penetrations of intermittent renewable energy sources on the supply side [42]. This means that part-load operation and transient operation, i.e. load changes and start-up, will be growing in significance for thermal power plants [31]. Furthermore, market demand target operational flexibility due to the continuing shift towards renewable power generation [43]. Simple but rigorous methodologies, e.g., dynamic process simulations including model validations [44], are needed to correctly predict the performance and to increase overall efficiencies. Dynamic modelling scenarios become indispensable for predicting dynamic interactions and performances of power plants to variable renewable energy sources.

Several studies focus on dynamic simulations of single critical parts of thermal power plants and post-combustion combined cycles with CO_2 capture (e.g., Refs. [43,45–52]), but, yet, very few on oxy-combustion CCS cycles. Latter studies are Refs. [53–57]. The only publication, which focuses on a natural gas fired oxy-combustion system is found in Ref. [57] analysing dynamic load changes of the Allam cycle. Pottman et al. [53] and Chansomwong et al. [54] present

dynamic simulations of a carbon dioxide purification unit (CO_2CPU) placed downstream of a coal fired oxy-combustion power plant. Luo et al. [55] performed a dynamic simulation of an oxy-combustion system (with coal as a fuel input) including model validation and transient analysis of typical operation parameters. Their aim was to improve control system design. Sachajdak et al. [56] presented a short review of methodologies that are generally applied for studying energy system transient behaviour. They used the process simulation tool Aspen Plus Dynamic on a CCS capable power plant. To the best of the authors' knowledge, none of these studies went into depth concerning power generation flexibility and plant ramp rates. Thus, the following research questions are allocated in the field of studying plant efficiency and plant flexibility.

1.3. Scope and key contributions

The novelty of this study lies in the assessment of transient load changes, and the conduction of a systematic dynamic modelling and simulation approach for the oxy-combustion Graz Cycle via improved off-design performance results. The investigation begins on design condition, moving over off-design condition and part-load operation to a dynamic environment. The cycle is optimised to meet highest plant efficiency at full-load and at part-load condition. At the final stage of this study, the detailed dynamic Graz Cycle model is used to answer whether this specific cycle is capable of doing rapid load changes in the context of high renewable energy penetrations. According to Domenichini et al. [58], the dynamic operation of oxy-combustion CCS power plants is limited by the ASU ramp rate, i.e., 3%/min. However, pure oxygen can be stored in times of low demand and thus it should not be seen as the bottleneck in the dynamic operation of such power systems. A good overview of the flexibility requirements of an energy system dominated by renewable energies is given by Kondziella et al. [59]. Within this context, this study should provide clearance whether the oxy-combustion CCS cycle can be operated in a dynamic manner and what the extent of balancing services is, which these units can provide to the energy system.

In short, the research question of this study is:

- Can oxy-combustion power plants with CCS provide balancing services to the electrical grid in the context of high renewable energy penetrations?

By answering this research question, this work provides a few important contributions and novelties, which are listed as follows:

(i) First dynamic simulation of the Graz Cycle and first off-design analysis including compressor maps with variable inlet guide vane (VIGV) schemes.

(ii) Overall, second study evaluating a dynamic simulation of an oxy-combustion power cycle. The first study of the kind is found in Fernandes et al. [57].

(iii) First work which explicitly develops a mathematical model catalogue for oxy-combustion power plants in dynamic operation.

(iv) Down to scale of an individual plant, this research paper aims to assess transient operations at a temporal scale of seconds to minutes, instead of an hourly resolution proposed by Fernandes et al. [57].

The rest of this research paper is organised as follows: Section 2 describes the process and the methodology, Section 3 describes the first-principle model of the digital twin, and Section 4 discusses the results of the different simulation scenarios. Finally, Section 5 provides the conclusive remarks and the ideas for future work. The modelling parameters are listed in Appendix A. Furthermore, Appendix B summarises the heat exchanger specifications and Appendix C provides a performance table.

2. Methodology

2.1. Description of the cycle

The following study builds on the Graz Cycle scheme presented for the first time in the year 2004 [27], further developed in 2005 [28] and assessed in 2022 [31] in the form of a part-load analysis. Fig. 1 shows the process scheme of the Graz Cycle, including the secondary plant controls evaluated in the previous study (see Ref. [31]). For the turbomachinery arrangement it is referred to Refs. [27–29]. The fuel and oxidant properties are listed in Table A.6. It is to be mentioned that for this study the oxygen purity is assumed to be 97%mol based on techno-economic analyses in Refs. [39,60].

In a nutshell, the principal reaction in the combustion chamber is chemically written as:

$$CH_4(g) + 2O_2(g) \longrightarrow CO_2(g) + 2H_2O(g), \qquad \Delta H_f^0(298 \text{ K}) = -604 \text{ kJ/mol}. \tag{1}$$
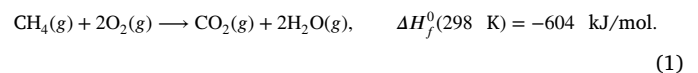
In this regard, the oxy-combustion process is described by the absence of nitrogen and other dilutants, which leads to a combustion flue gas composed of carbon dioxide and water; this is then condensed and pure carbon dioxide is further processed. The combustion gases drive a high temperature turbine and subsequently a generator. Similar to combined cycles, the flue gas exiting the turbine is used to heat a water stream due to its high temperatures. After cooling down, the rest of the working fluid is compressed and recycled to the combustor. Whereas a part of the working fluid is split to use the high enthalpy in a low pressure turbine. After expansion, the stream is condensed and the water is separated as aforementioned. Meanwhile the carbon dioxide content of the working fluid is further compressed (cf. "Exhaust CO_2" in Fig. 1) and then processed in the CO_2CPU accordingly, the feed water is pumped into the cold side of the HRSG. Here, as temperature increases throughout the bundles, it is forwarded to the high pressure turbine and (a split stream) to the low pressure steam turbine. A part of the water stream is used to cool the turbine blade stages, the other part keeps the combustion chamber at constant temperature. At this point, the cycle restarts by feeding the oxidant and the natural gas stream to the combustor.

The capture rate of oxy-combustion cycles is ideally 100%. In practice, the ASU is penalised by an air vent, which slightly decreases both the capture rate and CO_2 retention from the atmosphere [39]. Furthermore, the basic parameters of the GC which are all default settings for the steady-state simulation are listed in Table A.7. For a better understanding, Fig. 1 shows the power island of the Graz Cycle. The ASU is assembled in front of the process and produces a pure oxygen stream. Moreover, the CO_2CPU is placed at the end of the supply chain and processes the carbon dioxide stream.

2.2. Approach of the study

Fig. 2 summarises the methodology for process modelling and simulation of the Graz Cycle power plant. The methodology is based on the three consequent steps: (a) steady-state design modelling and simulation in Zone I; (b) steady-state off-design modelling and simulation in Zone II; and (c) dynamic modelling and simulation of the process in Zone III. The information flow goes from left to right by increasing detail and complexity. The process modelling goes hand in hand with the scenario generation in the simulation environment. The three steps follow from a higher to a lower (and more precise) layer:

- Zone I is based on Ref. [28]. More precisely, the steady-state design model is based on the version of the Graz Cycle concept first presented in the year 2005. Furthermore, the steady-state GC design model is adapted from the software's model database. The default parameter inputs for the simulation are summarised
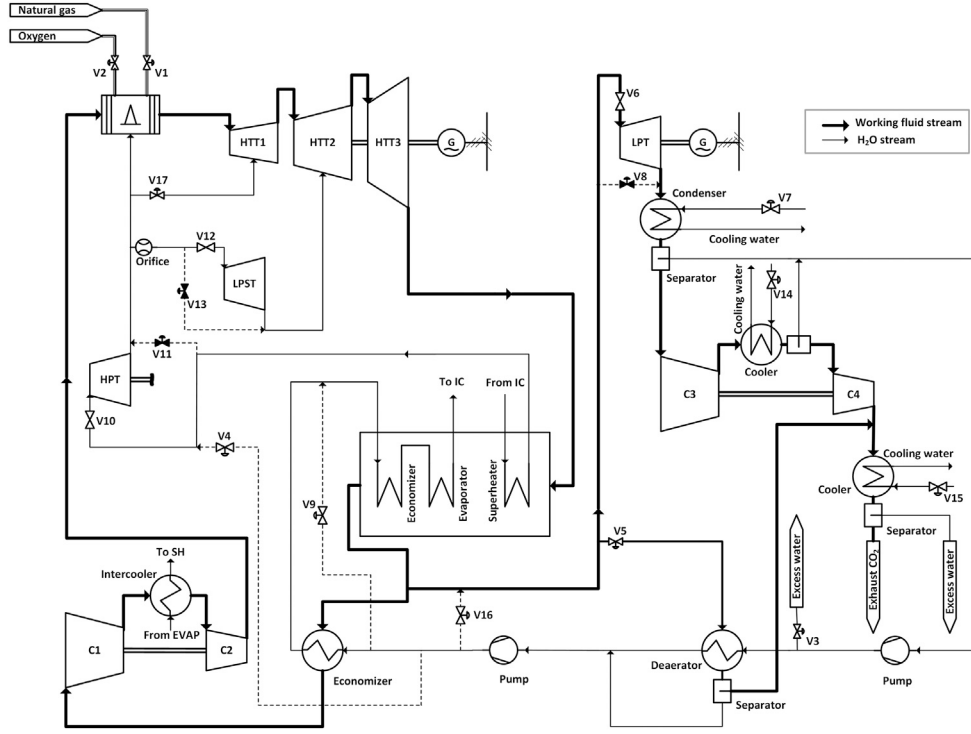
Fig. 1. Simplified process flow scheme of the Graz Cycle power island with carbon capture. Valves are labelled. Figure reproduced from Ref. [31].

in Tables A.6, A.7 and A.9. As a next step, the design-point simulation is performed to obtain the full-load scenario. In this regard, the objective function is written as:

$$\max_{\eta_i, \zeta_c, LHV} \quad \eta_{net} = \frac{\left(\sum P_{T,i} - \sum P_{C,i}\right)\eta_m \eta_G \eta_{Tr} - \frac{\sum P_{P,i}}{\eta_m} - P_{Aux} - P_{ASU} - P_{C,ASU} - P_{CPU}}{Q_{in}\left(1 + \zeta_c\right)},$$

$$\forall i \in [1, 2, \ldots, N]$$

s.t. steady-state mass and energy balances

design and off-design component models in IPSEpro

with $Q_{in} \geq 0$

for given $\eta_i, \zeta_C, m_{fuel}$.

(2)

- Zone II is based on Ref. [31] and is replicated with new modelling assumptions in this study. The off-design GC modelling comprises the finding of a fitting compressor performance map (normalised mass flow rate versus efficiency) to approximate its part-load behaviour. For this, under the compressor design modelling assumptions, the generated compressor maps are manually processed in a way that the operating lines are charted based on the off-design results obtained in a previous scenario run. The cutting points of the operating line and the efficiency lines are extracted and reproduced in dots in Fig. 3. As a final step, these single points are approximated by a polynomial function and employed as a "free equation" in the process simulation environment. The procedure of fitting compressor maps, including variable inlet guide vanes, is described in-depth by Ref. [61] and these guidelines are applied to this study. Subsequently, for steady-state off-design, the model is explained in Section 3.2 for the turbomachines. For the heat exchangers, the correlations described by Ref. [31] are applied. Table 3 evidences the efficiency assumptions hereby. The most efficient control strategy is selected for further processing in the subsequent dynamic scenarios. It

is to be noted that the control structures are adapted from the previous study. As indicated in Fig. 2, the green diamond reports the model-to-model validation. This means that the model is only led to the next stage if the off-design models operated at full-load match the design model at nominal load.

- Zone III represents the novelty of this study. To build up the dynamic model, the steady-state off-design model is employed and unit-by-unit replaced with the dynamic models equations. As a next step, the dynamic simulation of the power cycle is performed: first, as a simulation of the component model in a constrained environment, then, the component model is added to the entire cycle simulation. In the final stage, the transient operation mode is modelled and simulated. The dynamic models involved are described in Section 3. Before the results of the dynamic simulation are obtained, the preliminary outcomes are compared in a model-to-model validation with the off-design results at a certain load level. More precisely, the dynamic simulation values of the variables are compared to part-load results in stable mode (i.e., after passing the stabilisation period). The operational objective is following:

$$\max_{t, R_r^*} \quad R_r(t) = \frac{dP}{dt} \leq R_r^*,$$

$$\forall t \in [1, 2, \ldots, T]$$

s.t. dynamic mass and energy balances

dynamic component models in IPSEpro

with $P \geq 0.5 P_0$

for given R_r^*.

(3)

Here, the critical ramp rate R_r^* limits the operational plant to do drastic load changes, which could affect the integrity of its sub-systems and diminish the overall lifetime of the plant. Recent studies [62] found out that natural-gas combined cycles have a limiting maximum load gradient corresponding to the gas turbine's ramp rate. They found out that thermal stresses in critical
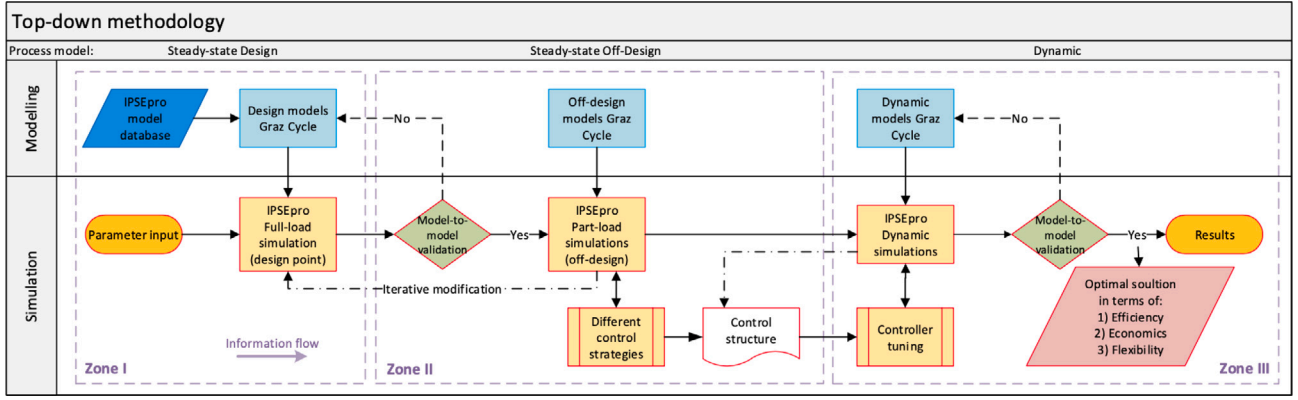
Fig. 2. Superstructure of the process modelling and simulation steps.

thick-walled components and auxiliary systems (e.g., the boiler) are not affected by rapid load changes. Thus, the gas turbine or, in case of the Graz Cycle, the high-temperature turbine is the bottleneck for very fast transient operation, at least when it comes to the inherent capability to do load changes in these power systems. In this study, the part-load performance of the Graz Cycle is limited to 50% of the nominal power output.

2.3. Software

For the process modelling and simulation, the software package IPSEpro v8 was used [63]. Accordingly, the modelling includes steady-state design and off-design methodologies, as well as dynamic equations. For the process modelling the system package MDK (Model Development Kit) was used. On the other hand, the software package PSE (Process Simulation Environment) was utilised to perform simulations and run different scenarios. The model-to-model validation is performed in the simulation environment of IPSEpro by switching between the different simulation stages and models discussed in Section 2.2. The natural distinction between modelling and simulation shown in Fig. 2 equates to the building environment of the software tool IPSEpro.

For the compressor modelling, the tool GasTurb v12 was employed to produce compressor maps including variable inlet guide vane schemes [64]. The applied assumptions are listed and discussed in Section 3.2. The results are subsequently transferred to Python for processing and analysing data to obtain e.g., the polynomial efficiency functions of the compressors.

3. Dynamic modelling

3.1. Process and heat exchanger models

In this study, a first-principle model of the Graz Cycle power plant was used to analyse the dynamic behaviour of its single components and of the whole cycle. The dynamic model catalogue for the digital twin of the power plant is developed in following part. Two balances are of utmost interest for this study: (a) the mass conservation balance, and (b) the energy conservation balance. Both balances can be expressed dynamically (i.e., in the form of a differential equation), or in steady-state (i.e., in the form of an algebraic equation) [65]. The two main equations are described in Eqs. (4) and (5):

$$\frac{dM}{dt} = \sum m_{in} - \sum m_{out}. \tag{4}$$

Here, the dynamic mass balance contains the (mass) holdup denoted as M. On the other hand side, the energy conservation law states following:

$$\delta W_t + \delta Q + \sum dm_i(h_i + e_{ex_i}) = dU + dE_{ex}. \tag{5}$$

In the dynamic modelling approach, the heat exchange equipment is firstly investigated since it represents the critical component in the dynamic scenarios. Heat exchangers dominate the dynamic behaviour and limit the transient operation of a power plant due to their large storage capacities. Assuming there is no water holdup in the tubes of the heat exchanger (i.e., no difference in the water mass flow rate between inlet and outlet), the dynamic equation for a control volume including gas, metal and water (in liquid state or steam) is defined in Eq. (11) in Table 2. To find the resulting three unknowns (i.e., gas exit temperature, water exit temperature and tube metal temperature), two additional heat transfer balances are used, i.e., Eqs. 7 and 9 [66]. The steam quality of the evaporator is set at the inlet (i.e., $x = 0$) as well as at the exit (i.e., $x = 1$), respectively. Furthermore, the area A_o of the single heat exchange units is assumed to be constant.

To sum up, the heat exchangers are modelled via a lumped parameter method. Yet, different equations result upon how boundary conditions are set. The yield is an energy balance for the tube, the wall (despite thermal resistance to heat transfer within the metal wall is neglected) and the shell. If needed, a control volume can be set around the margin of the whole system such that overall four differential energy equations result, i.e. one for each control volume. In Table 2, the subscripts L denote the liquid state of the fluid in the tube, and G the gaseous state, respectively. T_m is the mean metal wall temperature.

Apart from that, the condenser and cooler are modelled with the off-design method, see Ref. [31]. More precisely, the condenser is modelled with tight pressure control, i.e., the condenser pressure remains constant and the cycle is open [67]. The cooler has three settings on the inlet condition of the cooling water coming from the sea or water reservoir. The assumption is, that the unit is large enough to prevent liquid mass holdup on the hot working fluid side.

For the calculation of the heat transfer coefficients, Kern's method is applied [68]. After an initial estimation of the volume of the tube masses, the tube-side heat transfer coefficient α_i is calculated by the empirical correlation:

$$\alpha_i = \frac{4200(1.35 + 0.02t)c_t^{0.8}}{d_i^{0.2}}, \tag{26}$$

where t is the mean water temperature in the tube, c_t is the mean velocity of the liquid in the tube, and d_i is the inner diameter of the tube.

Accordingly, the shell-side heat transfer coefficient α_0 is calculated via the Nusselt number:

$$Nu = \frac{\alpha_o d_o}{\lambda_o} \qquad \text{and} \qquad Nu = j_h RePr^{\frac{1}{3}} \left(\frac{\mu}{\mu_w}\right)^{0.14}, \tag{27}$$

Table 2

First-principle model of the heat exchange equipment. Here, M stands for mass conservation balance, E for energy conservation balance, H for heat transfer balance and B for boundary condition. As required, the control volume can be set around the shell-side, the tube-side, the metal wall and the whole heat exchanger section.

Component	Control volume	Equation		Balance			
		nr.	Description	M	E	H	B
Economisers and intercooler	Shell-side	(6)	$\frac{dM_G}{dt} = 0 = m_{G,in} - m_{G,out}$	x			
		(7)	$m_{G,in}h_{G,in} - m_{G,out}h_{G,out} = \alpha_o A_o(\overline{T}_G - T_m)$		x		
	Tube-side	(8)	$\frac{dM_L}{dt} = 0 = m_{L,in} - m_{L,out}$	x			
		(9)	$m_{L,in}h_{L,in} - m_{L,out}h_{L,out} = \alpha_i A_i(\overline{T}_L - T_m)$		x		
	Metal wall	(10)	$\alpha_o A_o(\overline{T}_G - T_m) = \alpha_i A_i(T_m - \overline{T}_L)$		x		
		(11)	$m_{G,in}h_{G,in} - m_{G,out}h_{G,out} = \frac{dH_m}{dt} + m_{L,out}h_{L,out} - m_{L,in}h_{L,in}$		x		
	Whole system	(12)	$\frac{dH_m}{dt} = \frac{\rho_m V_m c_m dT_m}{dt}$		...		
		(13)	$\frac{1}{kA_o} = \frac{1}{\alpha_o A_o} + \frac{1}{\alpha_i A_i}$			x	
		(14)	$\frac{dT_m}{dt}\big|_{t=0} = 0$				x
Evaporator	Shell-side	(15)	$\frac{dM_G}{dt} = 0 = m_{G,in} - m_{G,out}$	x			
		(16)	$m_{G,in}h_{G,in} - m_{G,out}h_{G,out} = \alpha_o A_o(\overline{T}_G - T_m)$		x		
	Tube-side	(17)	$\frac{dM_L}{dt} = m_{L,in} - m_{S,out}$	x			
		(18)	$m_{G,in}h_{G,in} - m_{G,out}h_{G,out} = \frac{dH_m}{dt} + \frac{dH_L}{dt} + m_{S,out}h_{S,out} - m_{L,in}h_{L,in}$		x		
	Whole system	(19)	$\frac{dH_m}{dt} = \frac{\rho_m V_m c_m dT_m}{dt}$		...		
		(20)	$\frac{dH_L}{dt} = \frac{M_L c_L dT_L}{dt}$		...		
		(21)	$T_m = T_{S,out}, \qquad T_L = T_{L,in}$				x
Superheater	Shell-side	(22)	$\frac{dM_G}{dt} = 0 = m_{G,in} - m_{G,out}$	x			
		(23)	$0 = m_G c_{p_G}(T_{G,in} - T_{G,out}) - Q_{ex}$		x		
	Tube-side	(24)	$\frac{dM_L}{dt} = 0 = m_{L,in} - m_{L,out}$	x			
		(25)	$\frac{dT_L}{dt} = \frac{1}{M_L}\left(m_L\left(T_{L,in} - T_{L,out}\right) + \frac{Q_{ex}}{c_{p_L}} \right)$		x		

where j_h denotes the heat transfer factor dependent of the tube arrangement and Reynolds number (i.e., Re=$\frac{cd_o\rho}{\mu}$). Besides, Eq. (27) also contains the Prandtl number (i.e., Pr=$\frac{c_p\mu}{\lambda_o}$). According to Ref. [68], the term $\left(\frac{\mu}{\mu_w}\right)^{0.14}$ can be assumed as equal 0.99 for low-viscosity fluids. In order to calculate the fluid thermal conductivity λ_o, the empirical equation for gases (Eq. (28)) is used.

$$\lambda_o = \mu_o\left(c_p + \frac{10.4}{M}\right) \tag{28}$$

As a final step, the overall heat transfer coefficient k is calculated using Eq. 13 and through initial steady-state simulation, the heat exchanger specification kA_o can be reduced to obtain the total area A_o. In order to get the volume of the metal masses V_m, the number of tubes n per heat exchanger section needs to be calculated. This can be done by calculating the area of one single tube. Subsequently, the obtained overall area of the tubes A_o is then divided by the area of one single tube per section. By doing so, the calculation of the total volume of tubes V_m is straightforward in order to yield the total metal mass per heat exchanger section as described in Eq. 12, i.e., metal specific density ρ_m times volume of tubes V_m.

After the computation of the dynamic heat exchanger models, the modelling approach handles the less critical turbomachinery components discussed in the next section.

3.2. Turbomachinery models

For simplicity reasons and due to empirical studies [69], the mass balances for all types of turbomachinery is written in algebraic form (it is assumed to be no mass accumulation of gas or liquid), cf. Eq. (4). Furthermore, the applied quasi-steady equations are listed as follows for gas turbine and compressor (Eq. (29)), steam turbine (Eq. (30)) and feedwater pump (Eq. (31)). These equations are a mathematical approximation to the component map of the turbomachinery unit in off-design condition.

The high temperature turbine (i.e., the turbine of a gas turbine) is modelled employing the chocked nozzle equation. Such as the gas turbine, the four compressors are modelled assuming a chocked nozzle:

$$\frac{m_{G,in}\sqrt{T_{G,in}}}{p_{G,in}} = \frac{m_{G,in_0}\sqrt{T_{G,in_0}}}{p_{G,in_0}}. \tag{29}$$

Table 3
Summary of cycle off-design modelling assumptions.

Parameters	Functions	
Relative off-design efficiency [η_R]	Value, equation	Reference
Compressor	cf. Eq. (32)	[61,64]
Gas turbine and combustor	constant equal 1.0	[36,71]
Steam turbine	function of the mass flow rates, cf. Ref.	[31]
Feedwater pump	function of the mass flow rates, cf. Ref.	[70]

On the other hand, the steam turbines are conventionally modelled by use of the Stodala equation:

$$m_{S,in}\sqrt{\left(\frac{p_{S,in_0}^2 - p_{S,out_0}^2}{T_{S,in_0}}\right)} = m_{S,in_0}\sqrt{\left(\frac{p_{S,in}^2 - p_{S,out}^2}{T_{S,in}}\right)}. \tag{30}$$

For the two feedwater pumps following mass flow rate and enthalpy correlation is valid [70]:

$$m_{L,in} = m_{L,in_0}\left(\frac{\varrho_{L,in}}{\varrho_{L,in_0}}\right)\left(\frac{n_p}{n_{p_0}}\right), \qquad \Delta h_{L,in} = \Delta h_{L,in_0}\left(\frac{n_p}{n_{p_0}}\right)^2, \tag{31}$$

where n_p is the rotational speed of a variable frequency drive pump. If this value is kept constant in the simulation, the correlation is simplified accordingly. For the compressor efficiency map following equations are derived:

$$\eta_{Ci,s} = \sum_{j=0}^{N-1} \Theta_{i,j}\mu_R^{(4-j)}, \qquad \forall i \in [1, 2, \ldots, 4] \qquad \text{where} \quad \mu_R = \frac{m_{Ci}}{m_{Ci,0}} \tag{32}$$

with

$$\Theta_{i,j} = \begin{bmatrix} -8.282 & 28.603 & -38.001 & 22.847 & -4.287 \\ -24.555 & 82.525 & -104.760 & 59.492 & -11.819 \\ 0 & 0 & -10.989 & 21.341 & 2.546 \\ 0 & 0 & -1.385 & 2.546 & -0.312 \end{bmatrix}. \tag{33}$$

Here, the subscript i indicates the respective compressor, and j the element of the polynomial function.

Fig. 3 shows the above mentioned correlations including the surge margin, i.e., $SM_{(P/P-1)}$. The formula for the surge margin is written as a function of the pressure ratios (i.e., π):

$$SM_{(P/P-1)} = 100 \cdot \frac{\pi_{surgeline} - \pi_{operatingline}}{\pi_{operatingline} - 1}. \tag{34}$$

The pressure ratio in off-design condition is derived from previous study and indicated in the plots such as e.g., $\pi = \pi_0$ for the compressor C1. More precisely, the specific compressor map are only valid for the corresponding pressure ratio. The deduction of the compressor maps is made using the GasTurb tool. The operating point with the component map was scaled for an optimum operating range of the axial compressors. Moreover, the input data to the GasTurb tool for the cycle design point is defined in Table A.8. In this regard, default values are extracted from the process simulation performed by Ref. [31], and from Ref. [27] for turbomachinery design parameters, respectively.

3.3. Model assumptions

The main modelling assumptions are summarised in Tables 3 and A.9 regarding off-design efficiency relations and component efficiencies, respectively. For a detailed analysis of the energy expenditures for the ASU and CO$_2$CPU, it is referred to Darde et al. [60]. However, it is worth mentioning that both units are modelled as a *black box* considering a linear behaviour of rated power per mass flow rate in part loads.

The efficiency of turbomachines, listed in Table A.9, are updated to state-of-the-art values compared to Ref. [31], in which efficiencies are applied according to Ref. [28]. Notably, applied assumptions are congruous to Refs. [39,72]. As an example, the isentropic efficiency of the two axial CO_2 compressors are set to 0.85 in comparison to

outdated 0.78 of previous publications of the Graz Cycle. Furthermore, the efficiencies of the feedwater pumps are enhanced to 0.85 according to Ref. [72]. For the rest, the parameters remained the same as in Refs. [28,31].

Table 3 indicates the isentropic efficiency correlations in off-design, i.e., $\eta_R = \frac{\eta_s}{\eta_{s,0}}$. For the steam turbine, apart from the mass flow rate function described in Ref. [31], a part-load efficiency correction considering the exit steam quality is implemented, that is, $\eta_{s,corr} = \eta_s - \frac{1}{2}\Delta x_e$ [73]. The relative feedwater pump efficiency η_R equals 0.8 for the mass flow ratio (i.e., $\frac{m}{m_0}$) 0.5 and 1.3, respectively. The efficiency curve is approximated by a spline curve in these points, see Ref. [70].

4. Result and discussion

4.1. Design-point simulation results

The increase in the GC efficiency at nominal operating conditions compared to Refs. [28,31] is due to manifold reasons. First, the maximum turbine inlet temperature is increased from 1400°C to 1500°C. Second, the oxygen purity of the oxidant carrier stemming from the ASU is enhanced from 95%mol to 97%mol. This increase is due to an optimal compromise between high efficiencies at plant level and relatively low economic costs [60]. Third reason is the increase of isentropic efficiencies of the compressors C3 and C4 and the two feedwater pumps compared to previous analyses of the Graz Cycle.

Overall, the changes in assumptions lead to an increase in the net plant efficiency from 53.1% (previous study, i.e., Ref. [31]) to 54.5% (this study). In this regard, it is referred to Fig. 4 and to Table C.12. Moreover, the Graz Cycle has similar performance results at full loads compared to the Allam cycle studied by Zaryab et al. [71], which shows a net plant efficiency of 54.9%. For the sake of completeness, it is mentioned that the applied default parameters for the Graz Cycle and Allam cycle compared in Fig. 4 are not the same. On the one hand, the oxygen purity for the Allam cycle (AC) is assumed to be 99.5% in aforementioned study. On the other hand, the compressors' isentropic efficiencies in nominal conditions are assumed to be 0.9. Since the four compressor stages employed in the AC configuration by Refs. [71,74] are of a radial compressor type, the attained results are evaluated as rather optimistic.

4.2. Off-design simulation results

In this study, the previous work of Ref. [31] is extended and analysed by filling the research gap of missing compressor maps and new modelling assumptions. For the bigger picture, the results of this work are compared with the previous part-load results of the Graz Cycle as well as the results of the Allam Cycle presented by Zaryab et al. [71]. The results are presented in Fig. 4 and complemented in Table C.12 for this study.

In Fig. 5 the compressor performance maps including VIGV schemes for compressor C1 and C3 are analysed. The most critical compressor from a perspective of load reduction is C2. At 65% loads, this specific compressor enters the 6% surge margin threshold, which indicates the remaining margin to the surge line. It is to be noted that common industrial compressors usually aim for a minimum surge margin of around 8%–10%. Compressor C1 reaches the critical surge margin at
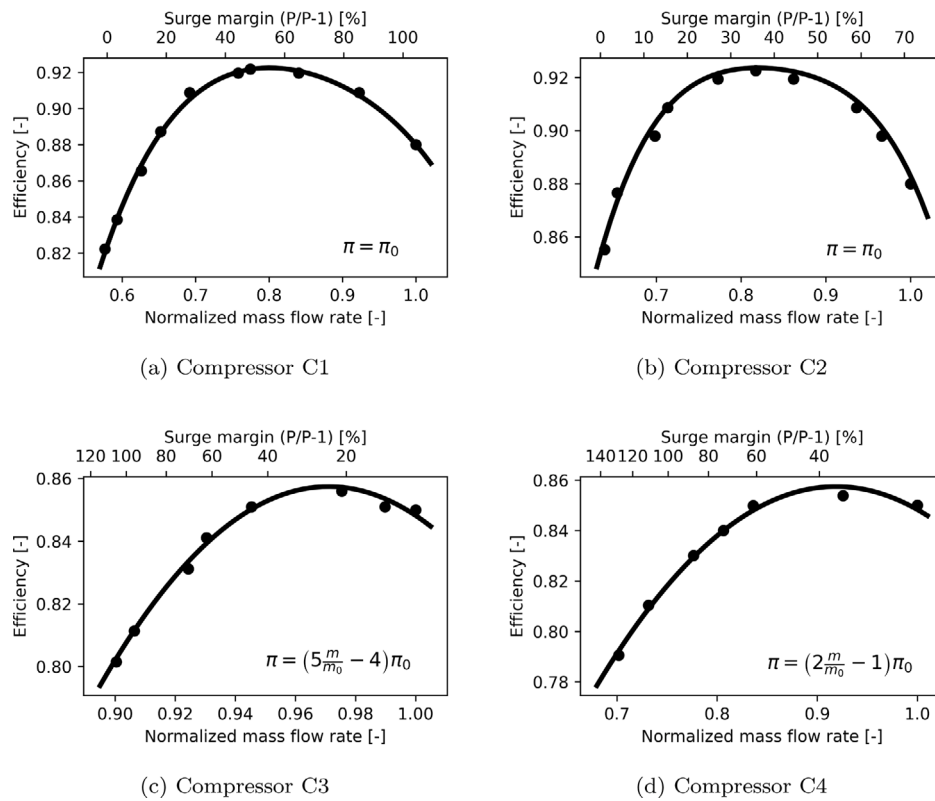
(a) Compressor C1

(b) Compressor C2

(c) Compressor C3

(d) Compressor C4

Fig. 3. The compressor performance maps derived through the GasTurb software. The dots indicate the values extracted manually from the compressor component map respective to the pressure ratio described in the bottom right corner.
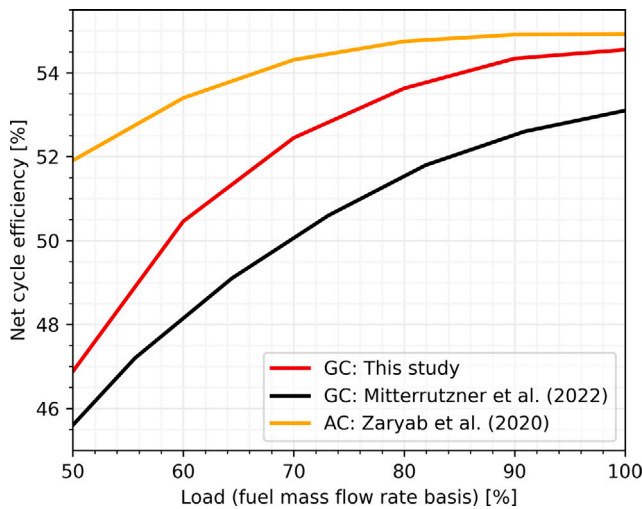

Fig. 4. Part-load performance results between this study and past publications. GC stands for Graz Cycle (Ref. [31]), AC for Allam cycle (Ref. [71]).

around 58% part load. However, at this load point the operational strategy needs to be changed such that touching the surge point is avoided. Therefore, the control strategy is altered at the critical load point of 65% as indicated in Table 4 from control strategy *A* to control strategy *B* as loads are decreased. In this case, the variable MV6 is changed from floating pressure control to throttle control. Accordingly, this leads to a stable pressure in the Benson boiler and, furthermore, this

reduces significantly the pressure ratio of the compressor C2 (compare Figs. 6(b) and 6(c)). As an effect the surge margin increases due to a decrease in the π-m map (i.e., the generated compressor component map with mass flow rate on the *x*-axis and pressure ratio on the *y*-axis). Consequently, the compressors C1 and C2 work in stable operation without surpassing the surge line. However, the downside of this control strategy change is that the slope in efficiency increases, see Fig. 6(a).

Figs. 6(d) to 6(f) analyse the cause of the relative efficiency decrease of control strategy *B* versus *A*. First of all, the recycled mass flow ratio (via compressor C1/C2) is significantly increased by the change of strategy from *A* to *B*. In turn, this leads to an increase in compression power for the specific stream, which is not sufficiently counteracted by the only relatively small increase in expansion work through the turbines (see Fig. 6(e)). On the other hand, the specific condenser heat release tends to penalise control strategy *B*, as shown in Fig. 6(d), i.e., the higher the heat rejection in the condenser and coolers, the lower the plant efficiency in accordance with the Carnot cycle.

After examining the key elements of the control strategy change, it is worth analysing the cause of the efficiency decrease of the power island through load reduction. One way to look at it is to investigate key trajectories of heat losses throughout the system. In this regard, as discussed in Fig. 5, the part-load performance of the compressors is transiently increasing. To sum up, the major players such as the HTT stages and the four compressors traverse a constant efficiency or even an efficiency increase via load reduction. Moreover, the O_2 generation and compression, and the CO_2 compression work after the purge valve remain approximately constant or have a temporary small increase in high load ranges, but overall have negligible effect on the plant efficiency. Therefore, the focus is set on the heat losses in the
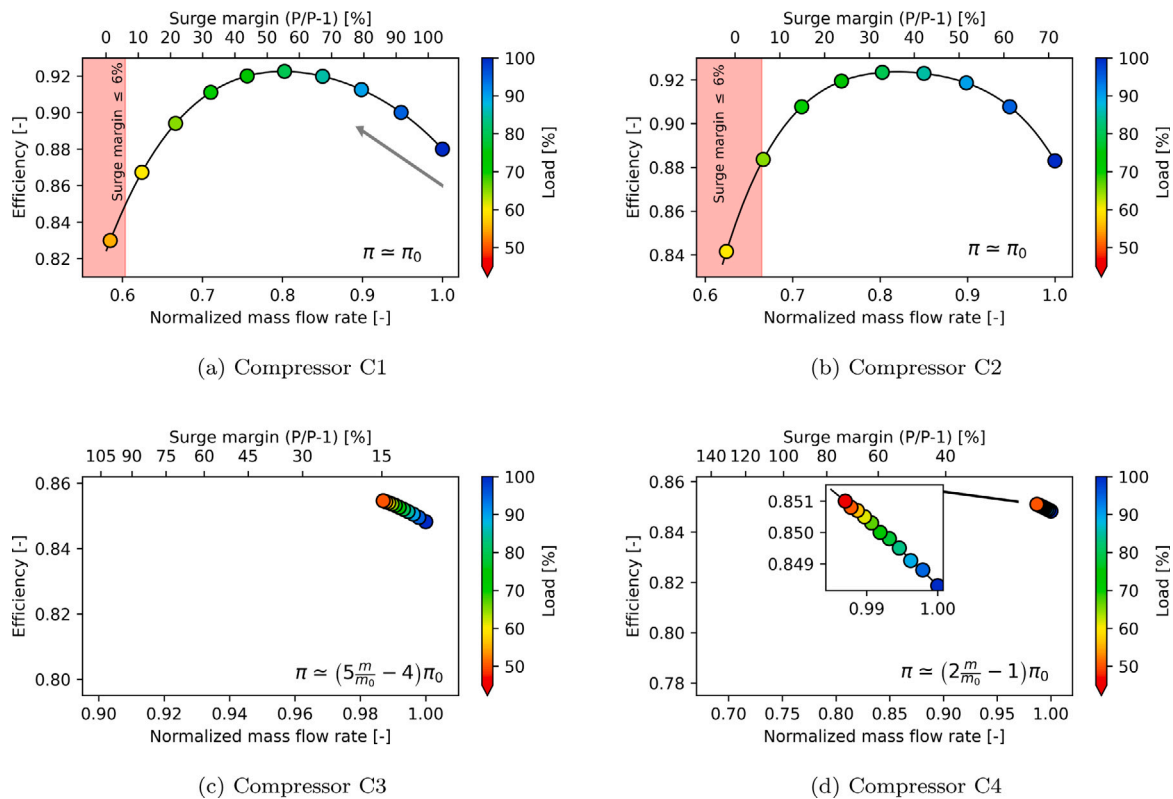
(a) Compressor C1

(b) Compressor C2

(c) Compressor C3

(d) Compressor C4

Fig. 5. The compressor performance maps including the operating line at different loads. The load reduction steps (on a mass flow rate basis) are set to 5% according to the process simulation. The scale of the compressor maps represent the whole operating range such as illustrated in Fig. 3.

system besides the heat rejection in the condenser (compare Fig. 6(d)). To some extent, the specific heat loss in the water purge valve has an influence by a temporary increase when load is reduced from full-load to around 60% part-load. However, the principal source of heat loss is the CO_2 purge trajectory in part loads, as indicated in Fig. 7. This drawback could be significantly reduced by another cooler unit, which leads to an efficiency enhancement through an increase of CO_2-purity as well as a decrease in specific heat losses. Another way to harness these excess energy is the employment of an organic Rankine cycle (ORC) or a heat pump (HP) system. In the former case, a secondary electricity surplus can be obtained and its configuration is for example studied by Ref. [75] for an Allam cycle power plant featuring liquified natural gas (LNG) as a fuel source. On the other hand, if a heat pump is implemented on the power island, an additional overall plant efficiency enhancement is achieved by provision of secondary district heat in an integrated energy system. For instance, this is studied by Ref. [76].

Some key learnings can be drawn from the above discussed results: (a) The off-design efficiency of the GC power plant is most efficient with variable boiler pressure control (in line with the findings of Ref. [31]); (b) However, at 65% part-load condition the control strategy has to be changed due to the compressor pair C1/C2 to prevent the step ahead the surge margin; (c) One major source of heat loss and hence plant efficiency reduction in part loads is the CO_2 purge valve; (d) This behaviour precludes an increase of the GC part-load performance despite favourable compressor maps, which reach their maximum efficiency at reduced loads.

4.3. Uncertainties in the dynamic modelling

The challenges regarding the process modelling and simulation of the Graz Cycle are related to the integrated structure of the cycle, where mass flow recirculations hinder a simple control and modelling

approach. The clear-cut between topping and bottoming cycle does not exist in contrast to common combined cycles fired with natural gas. Therefore, the merged process leads to a difficult handling in its operational patterns and the dynamic simulation needs to be simplified to overcome these hurdles. For example, not every system unit is modelled in a differential form as discussed in Section 3, but some components are left in algebraic form.

Nevertheless the steam turbines are generally modelled by the Stodola equation, the LPST model is approximated by the chocked nozzle equation in order that the equations in the process simulation are solvable. In the following section, a closer look into the model validation unveils the inaccuracies and difficulties encountered in the process simulation. It is anticipated that one obstacle encountered during the dynamic simulation is the steam evaporator mass holdup, which does not exhibit a stable behaviour at any time, notwithstanding that other parameters become constant after a certain settling time. This is shown for example in Fig. 8(e).

4.4. Model-to-model validation

Ideally, the applied dynamic models should be validated against measurements of specific variables in a reference plant. However, one valid way to prove the reliability of the dynamic model is to compare it to high-fidelity models such as steady-state models for design and off-design states. In this study, the focus of validation is identified and set to be the heat exchangers and primarily the heat recovery steam generator, i.e., a once-through Benson boiler. In this regard following paragraphs summarise the findings of the validation process of this bulky equipment.
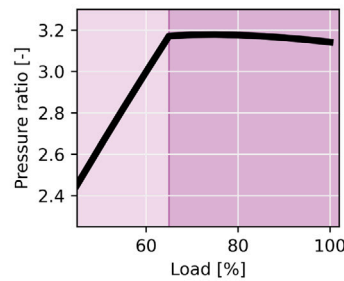
Table 5 shows the model-to-model validation between steady-state off-design and the dynamic model. The most significant deviations from the steady-state model are found in the parameters turbine exhaust
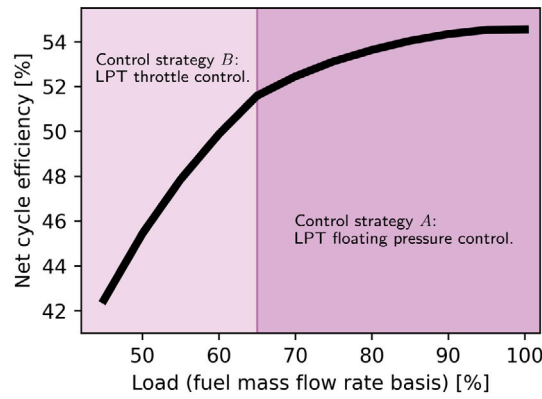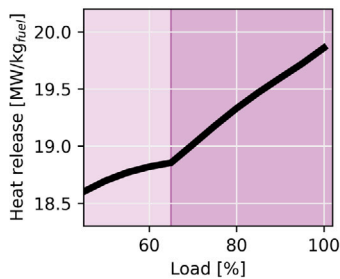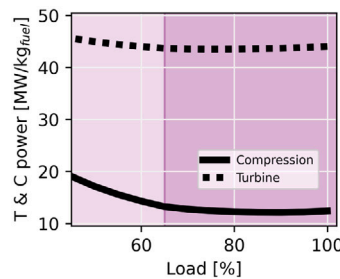
(a) GC part-load performance
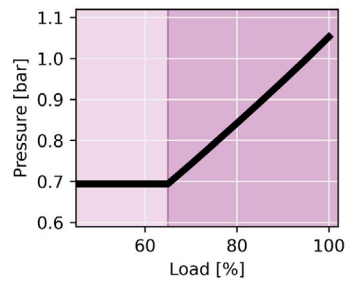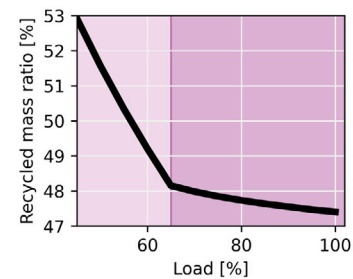

(b) HTT outlet pressure

(c) C2 pressure ratio

(d) Specific condenser heat release

(e) Specific turbine and compression power

(f) Recycled C1/C2 mass flow ratio

Fig. 6. Graz Cycle performance under different load conditions including a change of control strategy at 65% loads. The figure comprises three hierarchical levels. The top level describes the plant efficiency of the power island and the impact of the change in control strategy. The second level explains the reaction of the system to the control strategy variation. The bottom level analyses the cause of the slope in efficiency for control strategy B versus control strategy A.

Table 4
Control strategy and input–output pairing.

Control strategy		CV-MV pairing	
Scenario	Load range	Controlled variable (CV)	Manipulated variable (MV)
A	100%–65%	CV6: LPT valve pressure drop (i.e., equal 0)	MV6: LPT valve (i.e., fully open)
B	65%–50%	CV6: HTT exit pressure (i.e., constant)	MV6: LPT valve (i.e., throttle control)

gas temperature (TET), the feedwater pump mass flow rate and the condenser heat release. At nominal load condition the differences are negligible. The power and mass flow rate differences are indicated in percentages, whilst temperatures and pressures are in the respective units. At 90% part load, the TET in both models indicate a temperature difference of approximately 55 K. This deviation exists despite a constant turbine inlet temperature (TIT). The lower absolute value in the dynamic simulation can be partly explained by increased cooling mass flow rates to the HTT in the transient operation. Since the cooling

stream to the HTT1 is set by a constant mass flow rate split ratio (realised in practice by an orifice valve), the increased cooling mass flow rates are explained by an increase in the feedwater mass flow rate by 12.33% at 90% load. In turn, that is explained by a higher condenser heat release as the load is decreased in the dynamic simulation environment. The increased enthalpy drop in the HTT due to a higher cooling rate does not impact the overall electric power output of the plant.

The discrepancy between steady-state and dynamic model results opens the door for new methodologies other than first-principle models,

Table 5
Model-to-model validation between steady-state off-design and dynamic model after stabilisation time.

| Load	Variable	Scenario		Difference
		Steady-state	Dynamic	
100%	Electric power output incl. losses [MW]	75.22	75.12	0.13%
	Turbine inlet temperature [°C]	1500	1500	0.00 K
	Turbine exhaust gas temperature [°C]	608.02	608.16	0.14 K
	Boiler pressure [bar]	1.05	1.05	0.00 bar
	Feedwater mass flow rate [kg/s]	18.40	18.40	0.01%
	Condenser heat release [MW]	41.17	41.15	0.05%
95%	Electric power output incl. losses [MW]	71.47	71.70	0.32%
	Turbine inlet temperature [°C]	1500	1500	0.00 K
	Turbine exhaust gas temperature [°C]	609.17	582.74	26.43 K
	Boiler pressure [bar]	1.00	1.041	0.041 bar
	Feedwater mass flow rate [kg/s]	17.35	18.40	6.05%
	Condenser heat release [MW]	37.94	40.56	6.91%
90%	Electric power output incl. losses [MW]	67.48	68.21	1.08%
	Turbine inlet temperature [°C]	1500	1500	0.00 K
	Turbine exhaust gas temperature [°C]	610.28	554.89	55.39 K
	Boiler pressure [bar]	0.95	1.033	0.083 bar
	Feedwater mass flow rate [kg/s]	16.38	18.40	12.33%
	Condenser heat release [MW]	34.93	40.01	14.54%
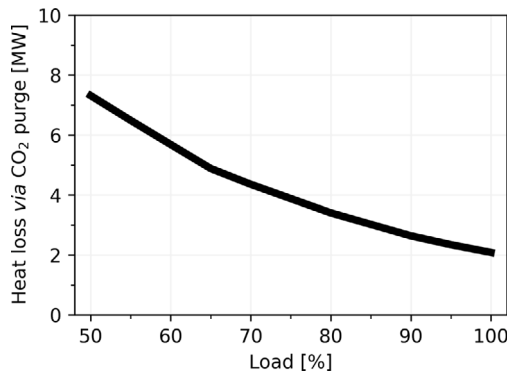
Fig. 7. Heat loss in the CO_2 purge valve under variable load conditions.

such as data-driven models. As emphasised by Formont and Nord [77], it is a very complex task to model a boiler in dynamic state with high accuracy. Instead of using a set of differential equations, they propose a data-driven method and artificial neural network algorithms.

In short, following conclusions can be drawn. The dynamic model shows to be very accurate at the 100% load point. TET indicates to be less precise when reaching part loads due to an increased feedwater mass flow rate and hence, dependent on that, a higher cooling mass flow rate to the high temperature turbine due to a set split ratio via the orifice valve (compare Fig. 1). The effect is that by an increase of the water mass content in the working fluid stream, the resulting condensation after the LPT results in a higher liquid water yield. This is also valid if the condenser heat release is actively set in the process environment. More precisely, the condenser after the LPT is controlled by a variable cooling stream such that the condenser pressure is kept constant. This dynamic behaviour is regarded as critical and effects a transient load decrease down to e.g., 80%. One possible solution could be that the cycle water outlet stream after the first feedwater pump is controlled though a water valve controller as designed previously by Ref. [31]. Overall, to increase the robustness of the process the transient load reduction is limited to a 10%-ramp and the deaerator, condenser and cooler are modelled by means of steady-state off-design equations.

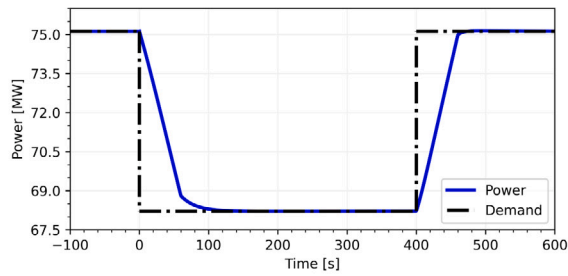### 4.5. Dynamic simulation results

In this study, the transient operation of the Graz Cycle is evaluated by means of different variable ramping rates. The aim is to evaluate

how quickly the power plant can react to load changes (e.g., by a scenario from full-load to 90%-load condition). This is called controlled process dynamics since it is in presence of supervisory and secondary control mechanisms. The exact hierarchical control structure of a power plant is further explained by Ref. [67]. The following paragraphs summarise the dynamic simulation results.

First, the step change profile which occurs at $t = 0$ s and $t = 400$ s is shown in Fig. 8(a). It represents, e.g., the set point coming from the electrical grid due to a lower demand of the end user. Fig. 8(b) presents the result of a transient load change of 10%/min. It shows, that the ramp cannot be followed exactly by the power plant but the system needs a settling time to stabilise and return to steady-state. The slope of the power reduction follows the slope of the fuel mass rate reduction until the rate is kept constant. At the setting of −10%/min fuel change the plant needs in total 140 s to reach steady-state conditions and deliver the exact amount of power output requested by the electricity system (i.e., in this study, the allowed discrepancy of total power output is 0.01 MW). In contrast, the setting of +10% leads to a very fast responding time, i.e., 13 s or an overall timeframe of 73 s for reaching a stable power output increase of 10%, see Fig. 8(b). The power increase or decrease can eventually happen even faster if the gas turbine (or in the case of the Graz Cycle, the HTT) over-shoots or under-shoots in relation to the set power output as shown by Rúa et al. [62] through a model predictive control adjustment. The rotary machinery in the Graz Cycle power plant possesses very fast system dynamics, i.e., the gas turbine, the compressors, the steam turbines and the feedwater pumps. Overall, this results in a very fast reacting power system.

In contrast, by taking into account that the gas turbine drives the transient operation, the boiler lags any kind of disturbance and slows down the load change. Concretely, the heat recovery steam generator consisting of ECO1, ECO2, EVAP, IC and SH is a bulky component with at its core large metal masses and slow heat transfer coefficients. Fig. 8(c) illustrates the fast dynamics of the gas turbine exemplified by the TET, and – in contrast – the slow heat transfer in the HRSG unit. As shown in light blue, the once-through boiler takes around 500 s to settle after a 10%/min load ramp.

Fig. 8(d) presents the decline of the boiler pressure at part-loads: firstly, an instant reaction to the fuel mass flow rate reduction, and then a slow reaction in the settling period. Regardless the fixed pressure losses in the HRSG, the reason for the latter behaviour is found in the increasing pressure drop of the HPT valve. The pressure drop causes a decrease of the feed pressure to the turbine and therefore a decrease of the drain pressure according to the Stodala equation.
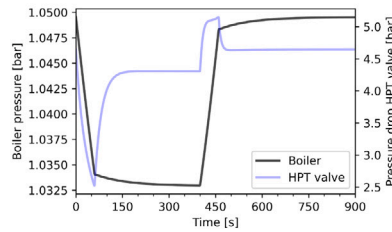
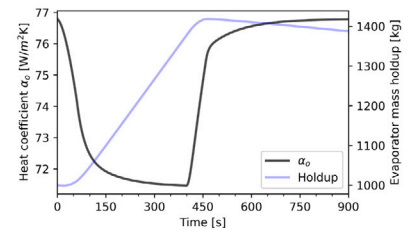(a) Definition of demand step change and corresponding load ramp rate
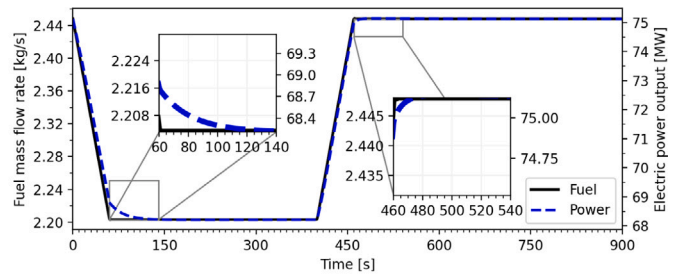
(b) Fuel and power
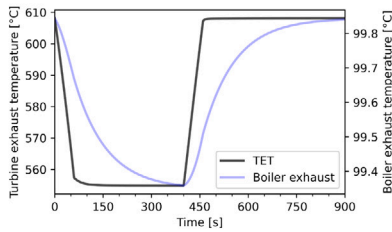
(c) Temperatures

(d) Pressures

(e) Evaporator

Fig. 8. Dynamic results of the simulation scenario. Setting equals to 10% load plant ramp in 60 s.

The evaporator, which is the section of the Benson boiler where the evaporation takes place, shows a constant increase in the saturated steam holdup to the point till the load is increased again (compare Fig. 8(e)). Furthermore, as shown in the figure, the fuel mass flow rate reduction effects an inert decline of the outer (i.e., the shell-side) heat transfer coefficient because of the drop in the flue gas mass flow rate. However, the increase in the load at $t = 400$ s causes a consequent instant ramp up of the heat coefficient. Thereby, it is evidenced that for the Graz Cycle it is easier to increase heat than to reject it due to the slow system inertia of the heat equipment (i.e., high heat retention and storage in the tube metal bundles). The tube-side heat transfer coefficient is very high such that the overall heat transfer coefficient is determined first and foremost by the outer coefficient α_o. This mathematical correlation is written in Eq. 13 and illustrated in Table B.10 for all once-through steam generator sections.

In a prompt manner due to an increase of the set load ramp rate, Figs. 9(a) to 9(d) show similar load change characteristics as explained above. It is to be said that the corresponding graphs are similar, but increases and decreases are faster including a few spikes due to the slow system inertia of the boiler in opposition to the fast dynamics of the turbomachinery (e.g., in Fig. 9(b)). Alongside the load change rate of 10%/min via fuel mass flow rate reduction (cf. Fig. 8), other investigated plant ramp rates are 20%/min and 60%/min (cf. plots in Fig. 9). Since the small rated power output of the plant, an aeroderivative gas turbine is used for the HTT. This component allows for load changes of up to 60%/min of rated capacity. As an example, in the case of the General Electric LM6000 aeroderivative gas turbine model, the maximum plant ramp rate is 30 MW/min for a net power output of 53 MW [78].

4.6. Assessment of balancing services for high penetrations of variable renewable energy sources in the power sector

As variable renewable energy sources gain to dominate the future power generation to the electrical grid, the intermittency in supply increases. Overgeneration of intermittent energy often results in curtailment, reduced environmental benefits and increased electricity costs [79]. The abundance of variable renewable energy can lead to the paradox situation of occasional negative electricity prices, as

experienced for instance in Germany in the past [80]. Thus, in the present and future rushed load ramp rates are required from power plants.

In this section, the timescales for load changes are minutes up to a few seconds. Following balancing services can be provided by fast responding power plants: time shifting, peak shaving, load levelling, and spinning reserve. Excluded are, among other things, ramping and load following, in which response time lies up to ~1 s, according to Ref. [81]. *Time shifting* comprises electricity storage when it is less expensive and electricity release during peak demand periods. This service can also be provided by dispatchable power plants through practising economic dispatch models as shown as an example in Ref. [82]. Followingly, *peak shaving* represents a similar concept. The operating principle is to store energy at off-peak periods to compensate for electricity demand at times, where maximum power is needed. Ref. [76] establishes this strategic regime for an oxy-combustion cycle via CO_2CPU, and Ref. [31] anticipates that charging and discharging modes of the ASU during different demand periods is key for balancing services. *Load levelling* describes the method of balancing fluctuations of intermittent renewable energy sources associated with power demand [81]. In this regard, Heuberger et al. [83] describe dispatchable CCS power systems as a cost-effective complement to fluctuating renewable energies, such as wind and solar. The application of *spinning reserve* entails a response time up to a few seconds and hence are on the limit of the practical ramp rate of oxy-combustion power systems. Spinning reserves are a function of contingency offered to the power system for example during a fast increase or decrease in power generation. This kind of application of energy storage systems is necessary in combination with the stochastic nature of wind and solar energy sources [84]. Henceforth, operational flexibility in thermal power plants (fired with natural gas) is vital and is assessed by three criteria: minimum complaint load, short start-up time and maximum load gradients to react quickly to necessities dictated by the electrical grid [17,43,62].

Fig. 10 summarises the operational flexibility measures of the Graz Cycle power plant. The practical load reduction rate – disregarding whether the set load ramp rate is 60%/min, 20%/min or 10%/min – is around 5%/min (i.e., 5.55%/min for a set load ramp rate of 60%/min). In contrast, for a load increase the fuel rate is important by reaching
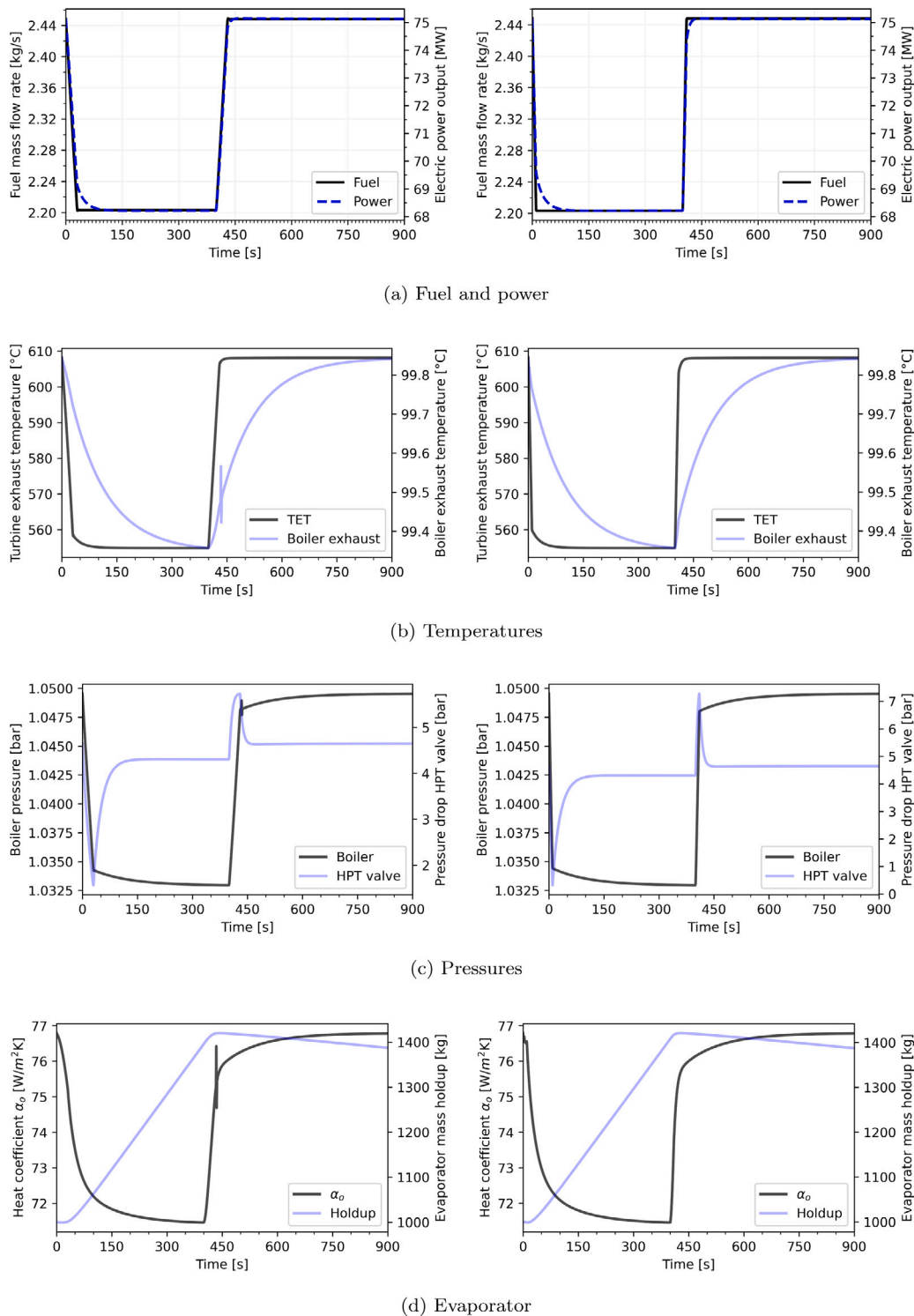
(a) Fuel and power

(b) Temperatures

(c) Pressures

(d) Evaporator

Fig. 9. Dynamic results of the simulation scenarios. Left, setting equals 20% load plant ramp in 60 s; Right, 60% ramp in 60 s, respectively.

very fast practical load ramp rates of up to 18.18%/min for a set load ramp rate of 60%/min. In comparison, the Graz Cycle power plant shows to handle negative ramp rates twice as fast as coal power plants, and positive ramp rates twice as fast than common combined cycle gas turbine power plants [85]. To conclude, considering that the plant's total power output is 75 MW, the transient load change characteristics can also be expressed in power per time. In this regard, the positive plant ramp rate is 13.6 MW/min and the negative plant ramp rate 4.2

MW/min, respectively. More precisely, while the GC load is ramping up, around 227 kW/s can be delivered to the electrical grid.

5. Conclusion

Renewable energy sources are the focal point for decarbonising the critical power generation sector. The variable nature of wind and solar energy carriers necessitates dynamic power assets with minimum complaint load and high ramping rates. In this regard, flexible power
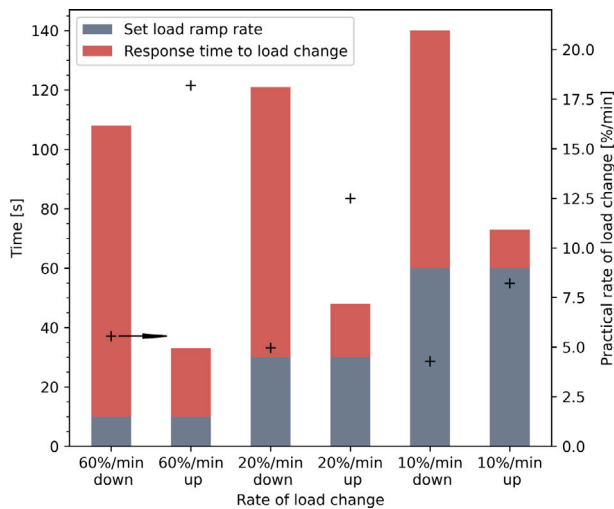
Fig. 10. Load change characteristics of the Graz Cycle power plant. Columns are related to the primary *y*-axis, and miniature crosses are related to the secondary *y*-axis.

Table A.6
Fuel and oxidant properties.

Parameter	Value
Natural gas quality [%mol]	
Methane	89.00
Ethane	8.11
Carbon dioxide	2.00
Nitrogen	0.89
Natural gas lower heating value [kJ/kg]	46,465
Oxygen purity and content [%mol]	
Oxygen	97.00
Argon	2.00
Nitrogen	1.00

(a) The dynamic capabilities of the Graz Cycle power plant is in-line with state-of-the-art combined cycles fired with natural gas. The Graz Cycle exhibits a practical negative load ramp rate of around 5%/min according to the process simulation.

(b) For load increase, the practical load ramp rate is even higher of up to 18%/min. This high load range is only achieved through aeroderivative gas turbines.

The model validation between dynamic and steady-state model results in relatively high discrepancies due to the complexity in modelling the boiler via first-principle models. Therefore, it is recommended that future work should include data-driven models in the dynamic simulation. Next to this, further work should analyse controls for the Graz Cycle including model predictive control strategies to be able to further decrease transient loads. In addition, a simple control logic for under- and over-shooting the gas turbine would significantly improve the load ramping rate. Finally, techno-economic studies investigating the profitability of oxy-combustion power plants at low loads should be carried out.

CRediT authorship contribution statement

Benjamin Mitterrutzner: Writing – original draft. **Lars O. Nord:** Writing – review & editing. **Mohammad A. Motamed:** Software. **Wolfgang Sanz:** Writing – review & editing.

Declaration of competing interest

The authors declare that they have no known competing financial interests or personal relationships that could have appeared to influence the work reported in this paper.

Data availability

Data will be made available on request.

generation in thermal power plants with carbon capture and storage enables carbon dioxide emission reductions and a promising alternative to energy storage as for instance large battery plants. This study presents results about the dynamic behaviour of the oxy-combustion Graz Cycle power plant. Ultimately, the question is answered whether oxy-combustion power systems can react quickly to load changes via fuel mass flow rate reduction and hereby provide balancing attendances to the electrical grid. Moreover, this study provides a novel dynamic modelling catalogue for an oxy-combustion carbon capture cycle, and a methodology how to best achieve dynamic simulation results via a stepwise modelling approach.

The achieved results are summarised in the following paragraph:

(i) The steady-state process simulation in nominal operating condition results in a net plant efficiency of 54.5%. This high efficiency is achieved at a oxygen purity of 97%mol and a maximum turbine inlet temperature of 1500°C. It includes the power consumption of the air separation unit and the carbon dioxide compression and purification unit.

(ii) Overall, the load is decreased in the off-design scenario down to 50% of the nominal value. The key outcome of the off-design analysis is listed as follows:

  (a) The off-design efficiency of the Graz Cycle power plant is most efficient with variable boiler pressure control (in line with the findings of Ref. [31]). However, the part-load performance in this study is significantly improved in comparison to previous study.

  (b) At 65% part-load condition, the control strategy is changed due to the compressor pair C1/C2 in order to prevent the step ahead the surge margin. The modelling of the four compressors includes specific component maps in variable inlet guide vane scheme operation.

  (c) One major source of heat loss and, thus, plant efficiency reduction in part loads is the carbon dioxide purge flow rate. This behaviour precludes an increase of the Graz Cycle part-load performance despite favourable compressor maps, which reach their maximum efficiency at reduced loads.

(iii) The dynamic analysis, performed on a high load range in between 90% and 100%, results in following insights:

Appendix A. Process modelling parameters

Tables A.6 to A.9 summarise the default modelling parameters set in the process simulation tools.

Appendix B. Heat exchanger properties

In Tables B.10 and B.11 the geometry details and properties of the heat exchangers is summarised, respectively.

Table A.7
Summary of Graz Cycle key design-point parameters.

Parameter	Value
Combustion pressure [bar]	40
Combustion heat loss, ζ_C [%]	0.25
Combustion temperature [°C]	1500
Combustion excess ratio, λ_C [-]	1.03
Heat recovery steam generator pressure loss p. heat exch. (cold side) [%]	3
Heat recovery steam generator pressure loss (hot side) [kPa]	4
Heat recovery steam generator minimum temperature difference (pinch point) [K]	5
Condenser pressure [bar]	0.041
Oxygen production in air separation unit [kJ/kg]	757
Oxygen compression in air separation unit (2.38 to 42 bar) [kJ/kg]	325
Carbon dioxide purification and compression (1 to 100 bar) [kJ/kg]	300

Table A.8
Design and off-design characteristics of the GC compressors as an input to the GasTurb tool.

Parameter	C1	C2	C3	C4
Pressure ratio, π [-]	13.529	3.133	6.050	7.104
Inlet corrected mass flow rate at design-point [kg/s]	34.718	34.718	9.492	7.104
Isentropic efficiency at design-point [-]	0.88	0.88	0.85	0.85
Total input pressure at design-point [kPa]	101.32	1331.00	4.13	24.24
Total input temperature at design-point [K]	375	664	291	298
Variable inlet guide vanes scheme [-]	Yes	No	Yes	No
Compressor inlet radius ratio [-]	0.6	0.65	0.6	0.6
Compressor inlet Mach number [-]			0.95	
Working fluid type [-]			Generic	

Table A.9
Main modelling assumptions and cycle design-point parameters.

Cycle design modelling parameters	Value
Vapour phase compressors isentropic efficiency (i.e., C1/C2), $\eta_{C,s}$	0.88
Carbon dioxide compressors isentropic efficiency (i.e., C3/C4), $\eta_{C,s}$	0.85
Feedwater pumps isentropic efficiency, $\eta_{P,s}$	0.85
High temperature turbine isentropic efficiency, $\eta_{T,s}$	0.9029
High pressure turbine isentropic efficiency, $\eta_{T,s}$	0.90
Low pressure turbine isentropic efficiency, $\eta_{T,s}$	0.88
Turbomachinery mechanical efficiency, η_m	0.99
Generator efficiency, η_G	0.985
Transformer efficiency, η_{Tr}	0.997

Table B.10
Heat recovery steam generator geometry data and nominal operating conditions.

Parameter	ECO1	ECO2	EVAP	IC	SH
Material	cupro-nickel	cupro-nickel	cupro-nickel	cupro-nickel	cupro-nickel
Tube specification	3/4 in. × 16 ft.	3/4 in. × 16 ft.	3/4 in. × 16 ft.	3/4 in. × 16 ft.	3/4 in. × 16 ft.
Outer diameter	20 mm	20 mm	20 mm	20 mm	20 mm
Inner diameter	16 mm	16 mm	16 mm	16 mm	16 mm
Length	4.83 m	4.83 m	4.83 m	4.83 m	4.83 m
Design heat exchange specification kA	78 kW/K	2,584 kW/K	316 kW/K	60 kW/K	221 kW/K
Design heat exchange rate	1,058 kW	26,002 kW	9,899 kW	2,709 kW	16,089 kW
Specific metal heat capacity	380 W/(m²K)	380 W/(m²K)	380 W/(m²K)	380 W/(m²K)	380 W/(m²K)
Tube metal density	8,940 kg/m³	8,940 kg/m³	8,940 kg/m³	8,940 kg/m³	8,940 kg/m³
Tube metal mass	6,070 kg	133,165 kg	40,465 kg	591 kg	16,863 kg
Tube metal volume	0.68 m³	14.90 m³	4.53 m³	0.07 m³	1.89 m³
Area outside (i.e., shell)	377 m²	8,275 m²	2,514 m²	37 m²	1,048 m²
Area inside (i.e., tube)	302 m²	6,620 m²	2,012 m²	29 m²	838 m²
Number of tubes	1,243	27,268	8,286	121	3,453
Heat transfer coefficient inside	31,595 W/(m²K)	63,670 W/(m²K)	83,453 W/(m²K)	83,645 W/(m²K)	101,700 W/(m²K)
Heat transfer coefficient outside	208.20 W/(m²K)	313.77 W/(m²K)	125.87 W/(m²K)	1,661.61 W/(m²K)	211.87 W/(m²K)
Overall heat transfer coefficient	206.83 W/(m²K)	312.23 W/(m²K)	125.68 W/(m²K)	1,629.25 W/(m²K)	211.43 W/(m²K)
Design (water) mass holdup	const.	const.	1000 kg	const.	1000 kg
Design mean water temperature in tube	56 °C	264 °C	367 °C	368 °C	462 °C
Design mean gas temperature in shell	83 °C	248 °C	419 °C	417 °C	536 °C

Table B.11

Nominal design properties of deaerator, condenser and cooler.

Parameter	Deaerator	Condenser	Cooler
Design heat exchange specification kA	193 kW/K	4180 kW/K	119 kW/K
Heat transfer coefficient inside	23,720 W/(m^{2}K)	15,461 W/(m^{2}K)	16,613 W/(m^{2}K)
Heat transfer coefficient outside	27,663 W/(m^{2}K)	8,656 W/(m^{2}K)	1,237 W/(m^{2}K)
Overall heat transfer coefficient	12,770 W/(m^{2}K)	5,549 W/(m^{2}K)	1,151 W/(m^{2}K)
Design (water) mass holdup	no holdup	no holdup	no holdup
Design mean water temperature in tube	56 °C	13 °C	19 °C
Design mean gas temperature in shell	83 °C	23 °C	173 °C
Process off-design modelling	steady-state	steady-state	steady-state

Table C.12

Performance table of the Graz Cycle with CO_2 capture.

Load at fuel mass flow rate basis [%]	Sanz et al. [28]	Mitterrutzner et al. [31]	This study Control strategy A								Control strategy B		
	100	100	100	95	90	85	80	75	70	65	60	55	50
Thermal cycle efficiency [%]	66.5	66.3	66.8	66.8	66.6	66.2	65.7	65.1	64.4	63.6	61.8	59.9	57.5
Net electrical cycle efficiency (incl. losses) [%]	64.6	64.4	66.0	66.0	65.8	65.4	64.9	64.3	63.6	62.8	61.2	59.3	57.0
Efficiency considering O_2-supply [%]	54.8	55.1	56.8	56.8	56.6	56.2	55.8	55.2	54.5	53.7	52.0	50.1	47.9
Net efficiency (incl. CO_2-compression) [%]	52.6	53.1	54.5	54.5	54.3	53.9	53.3	52.6	51.8	50.9	49.1	47.0	44.5
HTT power [MW]	120.27	95.49	90.19	85.37	80.72	76.15	71.63	67.15	62.75	58.44	54.19	49.96	45.76
Relative HTT load [%]	100.0	100.0	100.0	94.6	89.5	84.4	79.4	74.4	69.6	64.8	60.1	55.4	50.7
Total turbine power [MW]	142.75	113.53	107.78	101.93	96.18	90.55	84.99	79.51	74.13	68.87	63.99	59.14	54.34
Total compression power [MW]	47.16	37.12	30.41	28.43	26.78	25.36	24.07	22.91	21.89	20.98	20.93	20.89	20.88
Electrical power output (incl. losses) [MW]	95.59	73.73	75.22	71.47	67.48	63.38	59.22	55.02	50.79	46.55	41.85	37.16	32.50
O_2 generation and compression [MW]	14.15	10.64	10.69	10.15	9.62	9.08	8.55	8.01	7.48	6.94	6.41	5.68	5.34
CO_2 compression to 100 bar [MW]	3.12	2.19	2.25	2.18	2.10	2.04	1.98	1.93	1.88	1.83	1.81	1.80	1.78
Net power output [MW]	78.32	60.90	62.28	59.14	55.76	52.26	48.69	45.08	41.43	37.78	33.63	29.68	25.38
Total heat input [MW]	143.44	113.75	113.75	108.26	102.22	96.64	91.07	85.50	79.45	73.88	68.30	62.73	56.70
CO_2-purity at the exhaust gas drain [%]	92.0	90.5	88.1	86.6	84.8	82.6	80.0	77.1	73.8	70.2	65.6	60.7	55.6
Fluid composition at HTT drain [mol%]													
H_2O	77.1	75.8	76.9	76.9	76.8	76.8	76.8	76.9	76.9	76.9	77.5	78.0	78.8
CO_2	22.2	22.0	21.5	21.6	21.6	21.6	21.7	21.5	21.5	21.5	21.0	20.6	19.9
N_2	0.2	0.6	0.4	0.4	0.4	0.4	0.4	0.4	0.4	0.4	0.4	0.4	0.4
O_2	0.4	0.4	0.5	0.5	0.5	0.5	0.5	0.5	0.5	0.5	0.5	0.4	0.4
Ar	0	1.1	0.6	0.6	0.6	0.6	0.6	0.6	0.6	0.6	0.6	0.6	0.6
HTT inlet temperature [°C]	1400.0	1400.0	1500.0	1500.0	1500.0	1500.0	1500.0	1500.0	1500.0	1500.0	1500.0	1500.0	1500.0
HTT exhaust gas temperature [°C]	579.4	568.7	608.0	609.2	610.3	611.5	612.5	613.3	613.7	614.7	602.8	589.1	573.2
HTT inlet pressure [bar]	40.0	40.0	40.0	37.9	35.9	33.9	31.9	30.0	28.0	26.1	24.3	22.5	20.7
HTT outlet pressure [bar]	1.053	1.053	1.053	0.998	0.946	0.895	0.845	0.796	0.747	0.694	0.694	0.694	0.694
HPT inlet temperature [°C]	549	554.1	552.4	552.8	551.0	549.9	548.9	548.0	547.1	546.7	538.3	527.7	514.1
HPT inlet pressure [bar]	180.1	185.1	179.8	173.9	163.9	154.5	145.4	136.6	128.0	119.4	113.9	108.3	102.4
LPT inlet temperature [°C]	216.1	203.2	120.3	124.1	123.8	123.5	122.9	122.0	122.7	117.5	127.8	138.7	150.4
LPT outlet pressure [bar]	0.041	0.041	0.041	0.041	0.041	0.041	0.041	0.041	0.041	0.041	0.041	0.041	0.041
C1/C2 pressure ratio [-]	41.2	41.2	41.2	41.2	41.3	41.3	41.4	41.4	41.4	41.7	38.9	36.2	33.5
C1 inlet temperature [°C]	96.7	102.2	100.2	102.0	101.1	100.2	98.8	97.0	94.7	90.2	101.6	113.7	126.5
HRSG pinch point [°C]	5.0	5.0	5.0	4.6	4.3	3.9	3.6	3.3	3.0	2.7	2.6	2.4	2.3
Recycled stream mass flow ratio[%]	55.1	53.7	47.4	47.5	47.6	47.7	47.8	47.9	48.1	48.2	49.2	50.3	51.5
Relevant mass flows rates [kg/s]													
Fuel mass flow	2.89	2.45	2.45	2.33	2.20	2.08	1.96	1.84	1.71	1.59	1.47	1.35	1.22
O_2 mass flow	11.55	10.07	9.88	9.38	8.88	8.39	7.90	7.41	6.91	6.42	5.92	5.43	4.93
CO_2 mass flow to storage	8.91	7.30	7.50	7.25	7.01	6.80	6.61	6.43	6.27	6.11	6.05	5.99	5.94
C1/C2 mass flow	45.29	34.72	27.69	26.26	24.91	23.61	22.33	21.08	19.85	18.56	18.27	17.99	17.69

Appendix C. Steady-state performance results

Table C.12 summarises the steady-state performance results at nominal and off-design condition.

References

[1] IPCC, Climate change 2014: synthesis report, in: R.K. Pachauri, M.R. Allen, V.R. Barros, J. Broome, W. Cramer, R. Christ, J.A. Church, L. Clarke, Q. Dahe, P. Dasgupta, et al. (Eds.), Contribution of Working Groups I, II and III to the Fifth Assessment Report of the Intergovernmental Panel on Climate Change, 2014.

[2] IPCC, Climate change 2021: The physical science basis, in: Contribution of Working Group I to the Sixth Assessment Report of the Intergovernmental Panel on Climate Change, Cambridge University Press, Cambridge, United Kingdom and New York, NY, USA, 2021.

[3] IEA, Net Zero by 2050, IEA, 2021, URL: https://www.iea.org/reports/net-zero-by-2050. (Accessed 24 June 2023).

[4] IEA, Electricity, IEA, 2022, URL: https://www.iea.org/energy-system/electricity. (Accessed 28 August 2023).

[5] M. Bui, C.S. Adjiman, A. Bardow, E.J. Anthony, A. Boston, S. Brown, P.S. Fennell, S. Fuss, A. Galindo, L.A. Hackett, et al., Carbon capture and storage (CCS): the way forward, Energy Environ. Sci. 11 (5) (2018) 1062–1176, http://dx.doi.org/10.1039/c7ee02342a.

[6] R.M. Montañés, M. Korpås, L.O. Nord, S. Jaehnert, Identifying operational requirements for flexible CCS power plant in future energy systems, Energy Procedia 86 (2016) 22–31, http://dx.doi.org/10.1016/j.egypro.2016.01.003.

[7] E. Pusceddu, B. Zakeri, G.C. Gissey, Synergies between energy arbitrage and fast frequency response for battery energy storage systems, Appl. Energy 283 (2021) 116274, http://dx.doi.org/10.1016/j.apenergy.2020.116274.

[8] A.M. Elberry, J. Thakur, A. Santasalo-Aarnio, M. Larmi, Large-scale compressed hydrogen storage as part of renewable electricity storage systems, Int. J. Hydrogen Energy 46 (29) (2021) 15671–15690, http://dx.doi.org/10.1016/j.ijhydene.2021.02.080.

[9] G. Venkataramani, P. Parankusam, V. Ramalingam, J. Wang, A review on compressed air energy storage–A pathway for smart grid and polygeneration, Renew. Sustain. Energy Rev. 62 (2016) 895–907, http://dx.doi.org/10.1016/j.rser.2016.05.002.

[10] J.D. Hunt, B. Zakeri, R. Lopes, P.S.F. Barbosa, A. Nascimento, N.J. de Castro, R. Brandão, P.S. Schneider, Y. Wada, Existing and new arrangements of pumped-hydro storage plants, Renew. Sustain. Energy Rev. 129 (2020) 109914, http://dx.doi.org/10.1016/j.rser.2020.109914.

[11] P. Denholm, M. Hand, Grid flexibility and storage required to achieve very high penetration of variable renewable electricity, Energy Policy 39 (3) (2011) 1817–1830, http://dx.doi.org/10.1016/j.enpol.2011.01.019.

[12] N. Javanshir, S. Syri, S. Tervo, A. Rosin, Operation of district heat network in electricity and balancing markets with the power-to-heat sector coupling, Energy 266 (2023) 126423, http://dx.doi.org/10.1016/j.energy.2022.126423.

[13] M.A. Gonzalez-Salazar, T. Kirsten, L. Prchlik, Review of the operational flexibility and emissions of gas-and coal-fired power plants in a future with growing renewables, Renew. Sustain. Energy Rev. 82 (2018) 1497–1513, http://dx.doi.org/10.1016/j.rser.2017.05.278.

[14] M.F. Hasan, M.S. Zantye, M.-K. Kazi, Challenges and opportunities in carbon capture, utilization and storage: A process systems engineering perspective, Comput. Chem. Eng. 166 (2022) 107925, http://dx.doi.org/10.1016/j.compchemeng.2022.107925.

[15] IEA, Global CO2 Emissions by Sector, 2018, IEA, 2018, URL: https://www.iea.org/data-and-statistics/charts/global-co2-emissions-by-sector-2018. (Accessed 28 August 2023).

[16] J. Rúa, M. Bui, L.O. Nord, N. Mac Dowell, Does CCS reduce power generation flexibility? A dynamic study of combined cycles with post-combustion CO2 capture, Int. J. Greenh. Gas Control 95 (2020) 102984, http://dx.doi.org/10.1016/j.ijggc.2020.102984.

[17] M. Bui, N. Mac Dowell, Effects of plant scale on flexible operation of amine-based CO2 capture processes, in: Proceedings of the 15th Greenhouse Gas Control Technologies Conference, 2021, pp. 15–18, http://dx.doi.org/10.2139/ssrn.3820843.

[18] IEA, CCUS in Power, IEA, 2021, URL: https://www.iea.org/reports/ccus-in-power. (Accessed 28 August 2023).

[19] Global CCS Institute, The Global Status of CCS - 2017, Global CCS Institute, 2018, URL: https://www.globalccsinstitute.com/wp-content/uploads/2018/12/2017-Global-Status-Report.pdf. (Accessed 28 August 2023).

[20] N. Khallaghi, H. Jeswani, D.P. Hanak, V. Manovic, Techno-economic-environmental assessment of biomass oxy-gasification staged oxy-combustion for negative emission combined heat and power, Appl. Therm. Eng. 196 (2021) 117254, http://dx.doi.org/10.1016/j.applthermaleng.2021.117254.

[21] C. Greig, S. Uden, The value of CCUS in transitions to net-zero emissions, Electr. J. 34 (7) (2021) 107004, http://dx.doi.org/10.1016/j.tej.2021.107004.

[22] K. Hansen, C. Breyer, H. Lund, Status and perspectives on 100% renewable energy systems, Energy 175 (2019) 471–480, http://dx.doi.org/10.1016/j.energy.2019.03.092.

[23] IEA, The Role of CCUS in Low-Carbon Power Systems, IEA, 2020, URL: https://www.iea.org/reports/the-role-of-ccus-in-low-carbon-power-systems. (Accessed 28 August 2023).

[24] B. Metz, O. Davidson, H. De Coninck, et al., Carbon Dioxide Capture and Storage: Special Report of the Intergovernmental Panel on Climate Change, Cambridge University Press, ISBN: 9780521866439, 2005.

[25] V. Becattini, P. Gabrielli, C. Antonini, J. Campos, A. Acquilino, G. Sansavini, M. Mazzotti, Carbon dioxide capture, transport and storage supply chains: Optimal economic and environmental performance of infrastructure rollout, Int. J. Greenh. Gas Control 117 (2022) 103635, http://dx.doi.org/10.1016/j.ijggc.2022.103635.

[26] H. Jericha, E. Gottlich, Conceptual design for an industrial prototype Graz cycle power plant, in: Turbo Expo: Power for Land, Sea, and Air, Vol. 3607, 2002, pp. 413–420, http://dx.doi.org/10.1115/gt2002-30118.

[27] W. Sanz, H. Jericha, M. Moser, F. Heitmeir, Thermodynamic and economic investigation of an improved Graz cycle power plant for CO2 capture, in: Turbo Expo: Power for Land, Sea, and Air, Vol. 41723, 2004, pp. 409–418, http://dx.doi.org/10.1115/1.1850944.

[28] W. Sanz, H. Jericha, F. Luckel, E. Göttlich, F. Heitmeir, A further step towards a Graz Cycle power plant for CO2 capture, in: ASME Paper GT2005-68456, 2005, http://dx.doi.org/10.1115/gt2005-68456.

[29] H. Jericha, W. Sanz, E. Göttlich, Design concept for large output Graz Cycle gas turbines, in: Turbo Expo: Power for Land, Sea, and Air, Vol. 42398, 2006, pp. 1–14, http://dx.doi.org/10.1115/gt2006-90032.

[30] W. Sanz, M. Braun, H. Jericha, M.F. Platzer, Adapting the zero-emission Graz Cycle for hydrogen combustion and investigation of its part load behavior, Int. J. Hydrogen Energy 43 (11) (2018) 5737–5746, http://dx.doi.org/10.1016/j.ijhydene.2018.01.162.

[31] B. Mitterrutzner, W. Sanz, L.O. Nord, A part-load analysis and control strategies for the Graz Cycle, Int. J. Greenh. Gas Control 113 (2022) 103521, http://dx.doi.org/10.1016/j.ijggc.2021.103521.

[32] F.A. Gutiérrez, L.M. García-Cuevas, W. Sanz, Comparison of cryogenic and membrane oxygen production implemented in the Graz Cycle, Energy Convers. Manage. 271 (2022) 116325, http://dx.doi.org/10.1016/j.enconman.2022.116325.

[33] L.O. Nord, O. Bolland, Carbon Dioxide Emission Management in Power Generation, John Wiley & Sons, ISBN: 9783527347537, 2020.

[34] R. Allam, S. Martin, B. Forrest, J. Fetvedt, X. Lu, D. Freed, G.W. Brown Jr., T. Sasaki, M. Itoh, J. Manning, Demonstration of the Allam Cycle: An update on the development status of a high efficiency supercritical carbon dioxide power process employing full carbon capture, Energy Procedia 114 (2017) 5948–5966, http://dx.doi.org/10.1016/j.egypro.2017.03.1731.

[35] P. Mathieu, R. Nihart, Zero-emission MATIANT cycle, 1999, http://dx.doi.org/10.1115/1.2816297.

[36] R.E. Ulfsnes, O. Bolland, K. Jordal, Modelling and simulation of transient performance of the semi-closed O2/CO2 gas turbine cycle for CO2-capture, in: Turbo Expo: Power for Land, Sea, and Air, Vol. 3686, 2003, pp. 65–74, http://dx.doi.org/10.1115/gt2003-38068.

[37] H.M. Kvamsdal, K. Jordal, O. Bolland, A quantitative comparison of gas turbine cycles with CO2 capture, Energy 32 (1) (2007) 10–24, http://dx.doi.org/10.1016/j.energy.2006.02.006.

[38] R. Bannister, R. Newby, W. Yang, Final report on the development of a hydrogen-fueled combustion turbine cycle for power generation, 1999, http://dx.doi.org/10.1115/1.2816310.

[39] IEAGHG, Oxy-Combustion Turbine Power Plants, International Energy Agency Greenhouse Gas Cheltenham, UK, 2015.

[40] R. Kehlhofer, F. Hannemann, B. Rukes, F. Stirnimann, Combined-Cycle Gas & Steam Turbine Power Plants, third ed., Pennwell Books, ISBN: 978-1-59370-168-0, 2009.

[41] M. Kanniche, R. Gros-Bonnivard, P. Jaud, J. Valle-Marcos, J.-M. Amann, C. Bouallou, Pre-combustion, post-combustion and oxy-combustion in thermal power plant for CO2 capture, Appl. Therm. Eng. 30 (1) (2010) 53–62, http://dx.doi.org/10.1016/j.applthermaleng.2009.05.005.

[42] C.F. Heuberger, I. Staffell, N. Shah, N. Mac Dowell, What is the Value of CCS in the Future Energy System? Energy Procedia 114 (2017) 7564–7572, http://dx.doi.org/10.1016/j.egypro.2017.03.1888.

[43] F. Alobaid, N. Mertens, R. Starkloff, T. Lanz, C. Heinze, B. Epple, Progress in dynamic simulation of thermal power plants, Prog. Energy Combust. Sci. 59 (2017) 79–162, http://dx.doi.org/10.1016/j.pecs.2016.11.001.

[44] M. Bui, N.E. Flø, T. de Cazenove, N. Mac Dowell, Demonstrating flexible operation of the Technology Centre Mongstad (TCM) CO2 capture plant, Int. J. Greenh. Gas Control 93 (2020) 102879, http://dx.doi.org/10.1016/j.ijggc.2019.102879.

[45] R.M. Montañés, N.E. Flø, R. Dutta, L.O. Nord, O. Bolland, Dynamic process model development and validation with transient plant data collected from an MEA test campaign at the CO2 Technology Center Mongstad, Energy Procedia 114 (2017) 1538–1550, http://dx.doi.org/10.1016/j.egypro.2017.03.1284.

[46] R.M. Montañés, N.E. Flø, L.O. Nord, Dynamic process model validation and control of the amine plant at CO2 Technology Centre Mongstad, Energies 10 (10) (2017) 1527, http://dx.doi.org/10.3390/en10101527.

[47] R.M. Montañés, G. Skaugen, B. Hagen, D. Rohde, Compact steam bottoming cycles: Minimum weight design optimization and transient response of once-through steam generators, Front. Energy Res. 9 (2021) 687248, http://dx.doi.org/10.3389/fenrg.2021.687248.

[48] N.E. Flø, H.M. Kvamsdal, M. Hillestad, Dynamic simulation of post-combustion CO2 capture for flexible operation of the Brindisi pilot plant, Int. J. Greenh. Gas Control 48 (2016) 204–215, http://dx.doi.org/10.1016/j.ijggc.2015.11.006.

[49] M. Bui, I. Gunawan, V. Verheyen, P. Feron, E. Meuleman, S. Adeloju, Dynamic modelling and optimisation of flexible operation in post-combustion CO2 capture plants-A review, Comput. Chem. Eng. 61 (2014) 245–265, http://dx.doi.org/10.1016/j.compchemeng.2013.11.015.

[50] M. Bui, P. Tait, M. Lucquiaud, N. Mac Dowell, Dynamic operation and modelling of amine-based CO2 capture at pilot scale, Int. J. Greenh. Gas Control 79 (2018) 134–153, http://dx.doi.org/10.1016/j.ijggc.2018.08.016.

[51] A. Lawal, M. Wang, P. Stephenson, O. Obi, Demonstrating full-scale post-combustion CO2 capture for coal-fired power plants through dynamic modelling and simulation, Fuel 101 (2012) 115–128, http://dx.doi.org/10.1016/j.fuel.2010.10.056.

[52] A. Benato, A. Stoppato, A. Mirandola, Dynamic behaviour analysis of a three pressure level heat recovery steam generator during transient operation, Energy 90 (2015) 1595–1605, http://dx.doi.org/10.1016/j.energy.2015.06.117.

[53] M. Pottmann, G. Engl, B. Stahl, R. Ritter, Dynamic simulation of oxyfuel CO2 processing plants, Energy Procedia 4 (2011) 951–957, http://dx.doi.org/10.1016/j.egypro.2011.01.141.

[54] A. Chansomwong, K. Zanganeh, A. Shafeen, P. Douglas, E. Croiset, L. Ricardez-Sandoval, Dynamic modelling of a CO2 capture and purification unit for an oxy-coal-fired power plant, Int. J. Greenh. Gas Control 22 (2014) 111–122, http://dx.doi.org/10.1016/j.ijggc.2013.12.025.

[55] W. Luo, Q. Wang, X. Huang, Z. Liu, C. Zheng, Dynamic simulation and transient analysis of a 3 MWth oxy-fuel combustion system, Int. J. Greenh. Gas Control 35 (2015) 138–149, http://dx.doi.org/10.1016/j.ijggc.2015.02.003.

[56] A. Sachajdak, J. Lappalainen, H. Mikkonen, Dynamic simulation in development of contemporary energy systems–oxy combustion case study, Energy 181 (2019) 964–973, http://dx.doi.org/10.1016/j.energy.2019.05.198.

[57] D. Fernandes, S. Wang, Q. Xu, D. Chen, Dynamic simulations of the Allam cycle power plant integrated with an air separation unit, Int. J. Chem. Eng. 2019 (2019) http://dx.doi.org/10.1155/2019/6035856.

[58] R. Domenichini, L. Mancuso, N. Ferrari, J. Davison, Operating flexibility of power plants with carbon capture and storage (CCS), Energy Procedia 37 (2013) 2727–2737, http://dx.doi.org/10.1016/j.egypro.2013.06.157.

[59] H. Kondziella, T. Bruckner, Flexibility requirements of renewable energy based electricity systems–a review of research results and methodologies, Renew. Sustain. Energy Rev. 53 (2016) 10–22, http://dx.doi.org/10.1016/j.rser.2015.07.199.

[60] A. Darde, R. Prabhakar, J.-P. Tranier, N. Perrin, Air separation and flue gas compression and purification units for oxy-coal combustion systems, Energy Procedia 1 (1) (2009) 527–534, http://dx.doi.org/10.1016/j.egypro.2009.01.070.

[61] J. Kurzke, I. Halliwell, Propulsion and Power: An Exploration of Gas Turbine Performance Modeling, Springer, ISBN: 978-3030093709, 2018.

[62] J. Rúa, R. Agromayor, M. Hillestad, L.O. Nord, Optimal dynamic operation of natural gas combined cycles accounting for stresses in thick-walled components, Appl. Therm. Eng. 170 (2020) 114858, http://dx.doi.org/10.1016/j.applthermaleng.2019.114858.

[63] Simtech, IPSEpro, Simtech, 2023, URL: https://www.simtechnology.com/cms/ipsepro-menu/ipse-pro. (Accessed 28 August 2023).

[64] GasTurb, GasTurb, GasTurb, 2023, URL: https://www.gasturb.de. (Accessed 28 August 2023).

[65] S. Skogestad, Chemical and Energy Process Engineering, CRC Press, ISBN: 9781420087550, 2008.

[66] T. Kim, D. Lee, S. Ro, Dynamic behaviour analysis of a heat recovery steam generator during start-up, Int. J. Energy Res. 24 (2) (2000) 137–149, http://dx.doi.org/10.1002/(sici)1099-114x(200002)24:2<137::aid-er568>3.3.co;2-s.

[67] C. Zotică, L.O. Nord, J. Kovács, S. Skogestad, Optimal operation and control of heat to power cycles: A new perspective from a systematic plantwide control approach, Comput. Chem. Eng. 141 (2020) 106995, http://dx.doi.org/10.1016/j.compchemeng.2020.106995.

[68] R. Sinnott, Chemical Engineering Design: Chemical Engineering Volume 6, Elsevier, ISBN: 978-0750665384, 2005.

[69] F. Alobaid, Numerical Simulation for Next Generation Thermal Power Plants, Springer, ISBN: 978-3-319-76233-3, 2018.

[70] M.A. Motamed, L.O. Nord, Assessment of organic rankine cycle part-load performance as gas turbine bottoming cycle with variable area nozzle turbine technology, Energies 14 (23) (2021) 7916, http://dx.doi.org/10.3390/en14237916.

[71] S.A. Zaryab, R. Scaccabarozzi, E. Martelli, Advanced part-load control strategies for the Allam cycle, Appl. Therm. Eng. 168 (2020) 114822, http://dx.doi.org/10.1016/j.applthermaleng.2019.114822.

[72] K. Wimmer, W. Sanz, Optimization and comparison of the two promising oxy-combustion cycles NET Power cycle and Graz Cycle, Int. J. Greenh. Gas Control 99 (2020) 103055, http://dx.doi.org/10.1016/j.ijggc.2020.103055.

[73] M. Jüdes, S. Vigerske, G. Tsatsaronis, Optimization of the design and partial-load operation of power plants using mixed-integer nonlinear programming, in: Optimization in the Energy Industry, Springer, 2009, pp. 193–220, http://dx.doi.org/10.1007/978-3-540-88965-6_9.

[74] R. Scaccabarozzi, M. Gatti, E. Martelli, Thermodynamic optimization and part-load analysis of the NET Power Cycle, Energy Procedia 114 (2017) 551–560, http://dx.doi.org/10.1016/j.egypro.2017.03.1197.

[75] H. Yu, T. Gundersen, E. Gençer, Optimal liquified natural gas (LNG) cold energy utilization in an Allam cycle power plant with carbon capture and storage, Energy Convers. Manage. 228 (2021) 113725, http://dx.doi.org/10.1016/j.enconman.2020.113725.

[76] M. Xie, S. Liu, L. Chen, Y. Zhang, Y. Wang, S. Xie, Y. Zhao, Techno-economic and environmental assessment of a novel co-generation system integrating heat pump with Allam cycle, Energy Convers. Manage. 277 (2023) 116606, http://dx.doi.org/10.1016/j.enconman.2022.116606.

[77] V. Formont, L.O. Nord, N-BEATS neural network structure for sub-critical boiler data-driven modelling, in: 2023 International Joint Conference on Neural Networks, IJCNN, IEEE, 2023, pp. 1–8, http://dx.doi.org/10.1109/ijcnn54540.2023.10191299.

[78] GE Gas Power, LM6000 Aeroderivative Gas Turbine, GE Gas Power, 2023, URL: https://www.ge.com/gas-power/products/gas-turbines/lm6000. (Accessed 28 August 2023).

[79] P. Denholm, T. Mai, Timescales of energy storage needed for reducing renewable energy curtailment, Renew. Energy 130 (2019) 388–399, http://dx.doi.org/10.1016/j.renene.2018.06.079.

[80] E. Fanone, A. Gamba, M. Prokopczuk, The case of negative day-ahead electricity prices, Energy Econ. 35 (2013) 22–34, http://dx.doi.org/10.1016/j.eneco.2011.12.006.

[81] X. Luo, J. Wang, M. Dooner, J. Clarke, Overview of current development in electrical energy storage technologies and the application potential in power system operation, Appl. Energy 137 (2015) 511–536, http://dx.doi.org/10.1016/j.apenergy.2014.09.081.

[82] H. Yu, L.O. Nord, C. Yu, J. Zhou, F. Si, An improved combined heat and power economic dispatch model for natural gas combined cycle power plants, Appl. Therm. Eng. 181 (2020) 115939, http://dx.doi.org/10.1016/j.applthermaleng.2020.115939.

[83] C.F. Heuberger, I. Staffell, N. Shah, N. Mac Dowell, Quantifying the value of CCS for the future electricity system, Energy Environ. Sci. 9 (8) (2016) 2497–2510, http://dx.doi.org/10.1039/c6ee01120a.

[84] F. Díaz-González, A. Sumper, O. Gomis-Bellmunt, R. Villafáfila-Robles, A review of energy storage technologies for wind power applications, Renew. Sustain. Energy Rev. 16 (4) (2012) 2154–2171, http://dx.doi.org/10.1016/j.rser.2012.01.029.

[85] J. Hentschel, H. Spliethoff, et al., A parametric approach for the valuation of power plant flexibility options, Energy Rep. 2 (2016) 40–47, http://dx.doi.org/10.1016/j.egyr.2016.03.002.